## *Solid-State NMR Studies of Ternary Alloys for use in Sodium-ion Batteries*

PARTRIDGE, ELIZABETH,ROISIN,MAI

# Solid-State NMR Studies of Ternary Alloys for use in Sodium-ion Batteries

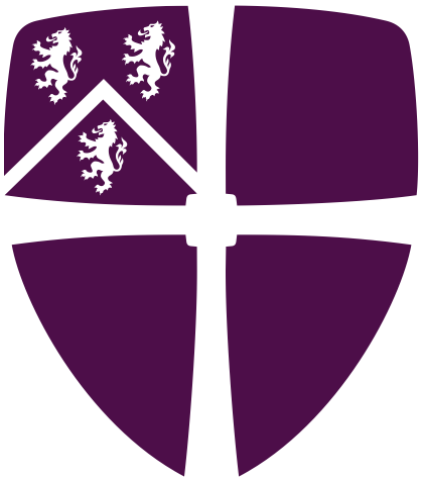

**Elizabeth Róisín Mai Partridge**

Department of Chemistry

University of Durham

This dissertation is submitted for the degree of

*Master of Science*

Trevelyan College 2019

# Abstract

Due to the pressures of climate change it is important to produce methods of renewable energy generation and storage which are cheap and can be applied to many industries and consumer needs. Sodium-ion batteries have proved viable alternatives to current Li-ion batteries, however they are unusable with graphite, which is the best negative electrode material we currently use. It is therefore important to develop other negative electrode materials which can perform to the same standards.

This research aims to investigate the performance of TiSnSb, a conversion negative electrode material, against sodium using electro-cycling and Solid-state Magic Angle Spinning Nuclear Magnetic Resonance (MAS ssNMR) to elucidate the chemical reactions which take place within the battery cells. Battery cells were constructed in a glovebox under an argon atmosphere, and data was obtained using a benchtop potentiostat and a Bruker 500.

Data was obtained for TiSnSb at C/2 and 4C rates for the first sodiation (discharge), first de-sodiation (charge), and second de-sodiation. C rate is defined as the number of sodium ions inserted per formula unit of TiSnSb per hour. Data was also collected for a rough mixture of Ti+Sn+Sb.

TiSnSb was found to operate via a conversion mechanism upon sodiation and de-sodiation with starting potentials of 2.6 – 2.8 V achieved consistently for multiple electrodes. In contrast Ti+Sn+Sb operates through an alloying reaction with multiple 'stages' of the reaction. The electrochemical rate has a strong effect on the number of Na ions inserted into the structure and the phases formed as evident from the potential profiles and MAS NMR spectra.

# Contents

# List of Figures

# List of Abbreviations

| Abbreviation | Explanation |
|---|---|
| CMC | Carboxymethyl Cellulose |
| CSA | Chemical Shift Anisotropy |
| CSR | Controlled Surface Reactions |
| DFT | Density Functional Theory |
| DMC | Dimethyl Carbonate |
| DNA | Deoxyribose Nucleic Acid |
| EC-DMC | Ethyl Carbonate-dimethyl |
| EFG | Electric Field Gradient |
| EMC | Ethyl Methyl Carbonate |
| eQ | Electric Quadrupolar Moment |
| ESS | Energy Storage Systems |
| EXAFS | Extended X-ray Absorption Fine Structure |
| FID | Free Induction Decay |
| FT | Fourier Transform |
| IL | Ionic Liquid |
| LiBOB | Lithium Bi-oxalatoborate |
| Li-ion | Lithium-ion |
| LTO | Lithium Titanium Oxide |
| MAS | Magic Angle Spectroscopy |
| MQMAS | Multiple Quantum Magic Angle Spectroscopy |
| NASICON | Sodium |
| NMR | Nuclear Magnetic Resonance |

| | |
|---|---|
| OCV | Open Circuit Voltage |
| PC | Propylene Carbonate |
| PNA | Peptide Nucleic Acid |
| SEI | Solid-Electrolyte Interface |
| SHE | Standard Hydrogen Electrode |
| SOLA | Solid Lineshape Analysis |
| ssNMR | Solid-state Nuclear Magnetic Resonance |
| VC | Vinylene Carbonate |
| VGCB | Vapour-grown Carbon Fibres |
| XRD | X-Ray Diffraction |

## Statement of Copyright



Elizabeth Róisín Mai Partridge

2019

# Acknowledgements

Thank you to my supervisor Karen for providing an endless and patient stream of support and advice.

Many thanks go to Tavleen, and Abby and the rest of the KEJ group for being so welcoming as well as helping and advising me whenever I needed assistance. I would also like to thank Dr Russell Taylor, Meera, Sam, and the rest of the RAT group for their optimism and abundance of jokes and smiles.

Finally, I would like to acknowledge the endless support of Trevelyan College and the MCR Community. In my one year as a postgraduate there I have made some of the strongest and most rewarding friendships and relationships of my life. The support from them has made this thesis possible.

Thank you to everyone who helped make this year happen.

# Chapter 1 Introduction and Literature Review

## 1.1 The Global Energy Situation

One of the largest scientific challenges is the race to tackle climate change. The mistreatment and pollution of the Earth is leading to global climate change via increasingly frequent disasters and extinction events. Hence, scientists must now work with global governance to introduce more benign and considered approaches to energy generation, manufacture, and other relevant industries.

There are a variety of sources from which energy is produced. Most energy is generated from the combustion of non-renewable sources *e.g.,* fossil fuels including oil, natural gas, and coal. However, burning fossil fuels as an energy source produces harmful greenhouse gases which have a negative impact on climactic temperatures and the Earth's ecosystem.[2] An alternative to using fossil fuels is to use renewable energy sources which are defined as a source that cannot be depleted with consistent use. Current sources of renewable energy include solar, hydro-electric, geothermal, and wind. The International Energy Association estimates that the total energy consumption as of 2015 was over 9000 Mtoe (Million tonne oil equivalents), with only 4% coming from renewable sources and 81.4% coming from fossil fuels.[3] This has risen to over 13000 Mtoe as of 2017 with only a 9% renewable contribution.[4] Since modern technology is strongly dependent on large amounts of energy, and that energy is being primarily provided from non-

renewable sources, the scientific consensus is that this is the driving factor behind the rapid degradation of the Earth's climate.[5]

A key issue with the use of renewable energy sources is that they are considered a fluctuating 'stream' of energy, *i.e.*, the output of energy from the source varies continually. Energy storage systems (ESS) are capable of accommodating and accounting for fluctuations in energy over time; this means they can provide electricity according to as and when it is needed. This is in direct comparison to regular distribution methods which are unable to store energy between generation and application. To successfully expand the integration of renewable energy into the commercial and industrial sectors it is necessary for ESS to cope with large-scale applications, whilst also remaining cheap to operate and produce.[6,1]

Electrochemical energy storage is the process of storing energy as chemical energy and converting it to electrical energy on demand. The most common form of energy storage is a battery, which is an ESS comprised of many electrochemical cells connected either in series or in parallel. These electrochemical cells exploit the oxidation and reduction of chemical species to store energy. Electrochemical energy storage systems are highly desirable because they reduce environmental pollution and increase battery cycle lives, whilst also providing a variety of low maintenance grid applications.[1] However, the cost of a battery system varies with the cell components and their availability. For example, lithium-ion (Li-ion) batteries (*vide infra*) are one of the most widely utilised battery types due to their high specific energy and high specific power (see Figure 1).[1] A battery's specific energy or gravimetric energy density defines the batteries capacity in terms of its weight (Wh / Kg) whereas specific power refers to the energy output (W) it is capable of delivering. Due to their superior battery performance, there is a high global demand for Li-ion batteries which has led to an overall increase in the cost of lithium as it is not

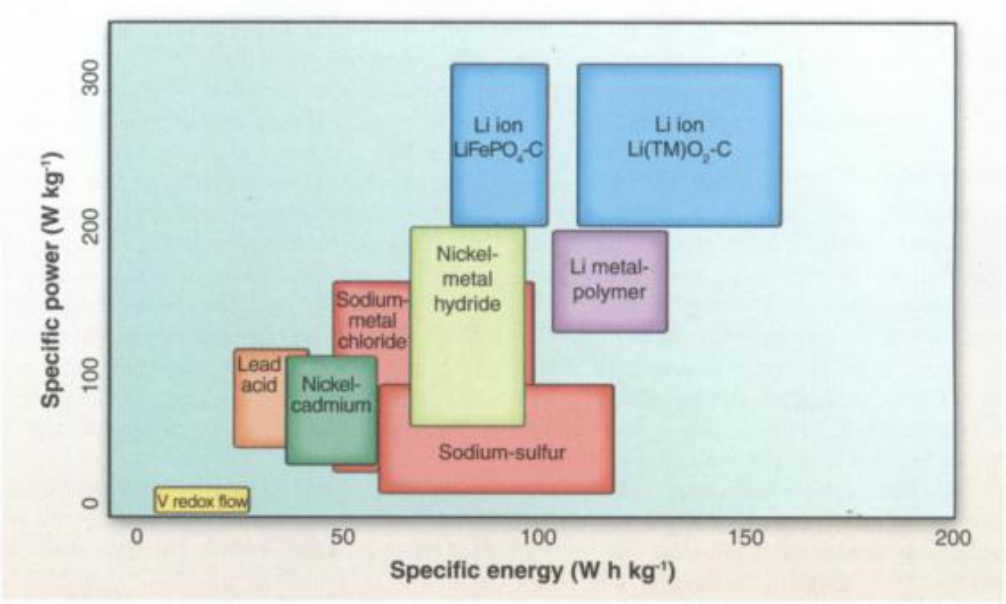


**Figure 1: Comparison of specific energy vs specific power for various rechargeable battery systems.[1] Reprinted with permission by AAAS.**

considered a naturally abundant metal (0.0017 % abundance).[6,7] Despite advances in extraction and mining methods the cost of lithium has continued to rise and was priced at $9,100 per ton in 2017, compared to $3,530 in 2007.[8] In 2008, with a global consumption of over 21000 tons, lithium usage was predicted to last a further 65 years.[9] Hence, this places pressure on the industry to develop new ways of excluding lithium from current battery systems.

Research into ESS is also highly important to commercial industries where the rise of portable electronics in the form of smart phones, personal computers, electric vehicles, and wearable electronics has led to an increase in the need for smaller, cheaper, safer, and more efficient ESS systems. Scientific research is therefore focused on developing low-cost alternatives to using Li-ion batteries that can deliver the same high-performance standards and cycle longevity needed for long-term commercial usage.

## 1.2 Batteries

A battery is composed of one or more electrochemical cells connected in parallel or in series where each cell is composed of three major components; two electrodes (the anode and the cathode), and the electrolyte. Within both batteries and cells, chemical energy is converted to electrochemical energy via redox reactions at each of the electrodes. The negative electrode (anode) is oxidised during the electrochemical reaction where the electrolyte acts as the ionic conductor and transports the charged ions produced at the anode to the cathode, which is then reduced.[10] This reaction is referenced as the discharge state of a battery/cell. During electrochemical cycling, electrons are forced to flow through the external circuit. The electrolyte is typically loaded onto a semi-permeable separator to prevent short circuiting. This separator is also an ion conductor but is an electrical insulator.

Primary batteries, also known as single use, generate electrical energy through the first and only discharge of cells from the stored chemical energy state into electrical output. Hence, once they have been fully discharged, they can be disposed of or suitably recycled. Secondary batteries can recover a charged state after the initial discharge where chemical energy is regenerated.[10] Rechargeable batteries can be restored to their charged state by passing a current in the opposite direction through the cell. Rechargeable batteries find their prime usage in modern portable electronics due to their reusability. These cells are also viable for ESS as they can be connected to a primary energy source to accommodate energy fluctuations and provide energy on-demand whilst also preventing unnecessary disposal.[10]

### 1.2.1 Evaluating Battery Performance

The cell potential of a battery is defined as the difference between the chemical potentials of the anode and the cathode. [10] Hence, the cell potential can be maximised by choosing electrode materials with a large difference in free energy.[11] The cell potential is affected by thermodynamic factors such as temperature, and kinetic factors such as concentration.

The theoretical capacity is an expression for the amount of electricity that can be transformed from chemical energy during redox. It is also possible to consider the cell in terms of theoretical energy (measured in watt-hours), which can be calculated as a product of the voltage by the capacity.[10]

However, in practice only a fraction of the theoretical characteristics are realised, this is often due to additional influences of the electrolyte and other nonreactive compounds present. The theoretical capacity assumes one hundred percent of the active material is involved in the redox reaction but this is often not the case due to electrochemical processes occurring during the first cycle, side reactions, or some material being utilised in the formation of the solid-electrolyte interface (SEI) formation (see section 1.2.3.1). Instead, it is common to evaluate cells in terms of their specific capacity, which equates to the capacity stored per unit mass or unit volume.

It is also very important to consider the energy density of the system when evaluating the storage capabilities; the gravimetric energy density (Wh $kg^{-1}$) and the volumetric energy density (Wh $L^{-1}$). In particular, it is important for portable rechargeable systems to have high volumetric and gravimetric energy densities in order to produce small and lightweight batteries.

Batteries can also be assessed in terms of their cycle- and shelf-lives. The shelf-life of a battery is defined as the amount of time it can remain charged and

idle without succumbing to self-discharge processes; where internal reactions reduce the capacity without a complete circuit being present. The cycle life is the number of full discharge/charge cycles a cell can undergo before the loss of capacity reduces to less than 80% of its original value.

The performance of batteries over long periods of time (*i.e*. 6 months or more) will always be subject to self-discharge processes, where the capacity of the cell decreases without actual usage. Rechargeable batteries tend to discharge anywhere from 2-30% across a period of a couple of months when compared to non-rechargeable batteries.[12] The shelf-life is particularly important for primary batteries, as rechargeable systems can be restored to a near-perfect capacity during a charge cycle. The cycle life is more important for rechargeable batteries, as irreversible capacity loss can be extremely detrimental to the system.

### 1.2.2 Electrode Classifications

#### 1.2.2.1 Intercalation Materials and Reactions

Intercalation electrodes are one of the most prominent electrode structural types currently used in rechargeable batteries, as they are capable of incorporating electroactive materials into a host network without destruction or rearrangement of the lattice/framework.[11] The redox reaction taking place is a solid-state reaction where chemical charge transfer occurs between the mobile metal-electrolyte ions and the electrode.[13]

Typically, electrodes are porous and/or microcrystalline, with a series of interconnected vacant channels in the structure, that are capable of hosting the mobile species. In the case of the rechargeable lithium-ion battery, the mobile species are the lithium ions. The ability to host a mobile charged species within a prebuilt framework with minimal volume expansion is the crucial advantage of

these materials as volume expansion of electrode species can result in unstable systems prone to combustion if in contact with air as many battery components can be pyrophoric. The lack or minimal volume expansion makes these great candidates for small commercial battery needs as they are a safer ESS.

When in the structure, the charged guest species can then move via the channels, thereby allowing charge transfer, and maximising the capacity of the electrode. During this intercalation process, the structure of the electrode remains mostly unchanged with only slight increases to the volume of the eternal structure this results in an electrode material capable of almost a fully reversible intercalation process. However, a consequence of the structural integrity of the electrode is that the potential curve will decline across multiple cycles.[14]

#### 1.2.2.2 Conversion Materials and Reactions

In recent years, conversion materials have become increasingly popular, owing to their high volumetric and energy densities. To date, there are several classes of conversion materials, including nano-sized transition metal oxides of cobalt, nickel and iron, as well as nano-sized lithium titanium oxides. Typically, conversion materials are composed of transition metal ions, and anions from the groups of either the chalcogens, halogens and, pnictides.[15,16] Electrochemical cycling of a conversion materials proceeds according to the following general mechanism,

$$M_xX_y + nyLi \leftrightarrow yLi_nX + xM + M_xX_y, \quad (1.1)$$

where M and X are the main components of the conversion electrode, *i.e.* the transition metal and the oxide or the other substituent and Li is the species being inserted.[15]

During a conversion reaction the active material undergoes a reversible reaction as it reacts with the guest ions (*e.g.* lithium), creating a series of highly

reactive lithiated compounds and metallic nanoparticles. These reactions involve the reduction of the active material, often to more thermodynamically stable species, across several intermediate steps.[15,17] Unlike intercalation electrodes it is not necessary for vacancies to exist within conversion materials and many materials deemed inappropriate for insertion electrodes have been found to yield better capacities when associated with the conversion process.[17,18] This is because the reaction mechanism taking place in each is very different.

Conversion materials are capable of incorporating more than one lithium atom per metal cation. Moreover, they typically possess very large theoretical capacities when compared to conventional carbon insertion materials.[15,19] In addition, they can operate over a wide range of potentials, which enables them to be used in a variety of different applications. Many of the materials used in conversion reactions also hold the advantage of being more abundant, affordable, and easily available compared to components for other electrode systems.[15]

Despite their many advantages, conversion materials have several drawbacks that inhibit their use. The most significant of which is that they possess a large voltage hysteresis.[17] This directly affects the discharge energy and can contribute to rapid heating of the system during battery operation.[15] The hysteresis can be directly observed in the charge/discharge profiles of the electrodes. This effect is most evident after the first discharge cycle and has been attributed to the structural differences between the crystalline pristine material and the amorphous compound formed after the first re-oxidation.[20]

It has been found that introducing a small amount of externally sourced cations and/or anions into the active material can favour an increase in conductivity, in particular with electrolyte species such as fluorides. For example,

Zhu *et al*. found that the conductivity of $FeF_3$ can be increased by adding a small amount of non-active Ti or N into the lattice.[15,17]

It has also been possible to increase the conductivity of oxide conversion materials such as CoO, MnO, and CuO by added a small quantity of $Li^+$ into the lattice, this addition jumps the initial reaction step by forming $Li_\alpha MO_{1-\beta}$ -type intermediates.[21] This affect has also been attributed to electrolyte decomposition, accompanied by formation of the SEI and reversible guest ion accumulation at the interphase between the lithium conversion products and the metallic nanoparticles.[15]

#### 1.2.2.3 Alloying Materials and Reactions

Electrochemical alloying is a process that can occur between the charge transfer species and metallic or semi-metallic elements. Most p-block elements are viable for alloying with alkali metals, particularly the metals and metalloids of group 4 and 5.[22] These elements have high capacities and, upon alloying, form alkali-metal rich compounds.

In a similar manner to conversion reactions, during alloying the structure of the host material is 'broken down', resulting in considerable structural changes.[23] As the host structure is changed and therefore does not constrain the reaction, alloying materials have higher theoretical capacities than standard intercalation materials. However, many of the species typically used in alloying reactions, such as Ga, Ge, Te, In, and Tl, are either too toxic or too expensive to be commercially used. Hence research has focused on some of the other elements within these groups.[22] Alloying reactions are also limited by the severe volume changes they undergo upon lithium insertion. In some cases, volume expansions can be as large as 440%. For example, in tin-containing species.[17]

The strategies for developing better alloying materials for rechargeable batteries have largely focused on designing new nano-structured materials, as well as the introduction of conductive carbon substrates and additives to try and counteract the reaction kinetics, voltage hysteresis, and volume expansion.[24] The addition of carbonaceous species such as graphene to alloying materials has been particularly successful, as graphene possesses a very high electrical conductivity, ensuring fast charge transfer, and acts as an inactive buffer, which helps to accommodate any volume expansion.[24,17]

### 1.2.3 Current Challenges in Battery Technology

#### 1.2.3.1 The Solid-Electrolyte Interface

The solid-electrolyte interface, or SEI, was a model initially proposed by Peled in 1979 to detail the formation of the interfacial layer that forms between the electrolyte and the negative electrode.[25] When cycled, non-aqueous lithium batteries develop a passivating $Li^+$ conducting film on the anode that is made of lithium carbonate (a biproduct of lithium reacting with the organic solvent in the electrolyte), and it was theorised that the existence of this film promoted stability and protected the metal electrode from further chemical attack.[26,27] Peled's model proposed that electrodes made of alkali or alkaline earth metals are always covered with this 15–25 Å layer at the surface, often composed of many insoluble compounds, e.g., LiF and $LiClO_4$ owing to the interaction of the metal electrode with the liquid electrolyte.

When electrochemically testing batteries, formation of the SEI is often evident owing to a notable drop in capacity between the 1$^{st}$ and 2$^{nd}$ discharge and a loss in reversibility. During the first discharge it is common for 10% of the capacity of the electrode to be lost.[28] Formation of the SEI is also known to limit the active surface area of the electrode by obstructing direct electrode-electrolyte

interactions. All of these drawbacks limit the rate of electrolyte deposition/integration, thereby acting as the rate-determining step ion migration.[29]

In order to be classified as SEI formation, rather than just a by-product on the surface layer, the SEI must also protect the electrode from direct and free contact with the electrolyte solution. Moreover, the SEI must function as a purely cationic conductor, *i.e.* electrons are not allowed to pass through the interphase.[25] Protecting the electrode from additional solvent interactions is essential as the intercalation of any additional solvent molecules to the electrode material can lead to disintegration of the electrode and increasingly large reductions in capacity, thereby limiting the life of the cell.[17] To optimise the SEI layer it is necessary for it to have negligible electrical conductivity and high electrolyte diffusion resistance to allow for high lithium-ion selectivity and permeability.[28] This optimisation is usually achieved using additives, for example maleimide additives and olefinic compounds.[30]

It is noted that the SEI layer will always form, independent of the precise composition of the anode, *i.e.*, it will not only form for alkali metals but also metalloids and metal oxides.[28] However, the volume expansion associated with these materials often leads to extensive and unstable SEI formation, as well as the rapid loss of capacity and mechanical degradation.[28]

#### 1.2.3.2 Volume Expansion

A key issue with the use of alloys and conversion materials is the introduction of metallic ions, which leads to a rapid expansion of the host material. For example, in the case of introducing lithium ions into a silicon anode there is an associated expansion of 280%, when Li is introduced into the structure.[22] Volume expansion introduces stress and strain into the system, and

on a cellular level the separator component can become crushed and the cell itself can bulge due to the addition of ions. Repeated expansion of the host material can also lead to loss of the electrical connection between the SEI and the electrode, resulting in cell fade, thereby preventing charge transfer and culminating in a loss of capacity. When the electrode material becomes electrically isolated, capacity fade is induced further.

Volume expansion of the active alloying material is the most significant factor in determining its suitability as an anode material. This overshadows a number of factors, including the impact of the materials energy density on the cycling performance of the compound.[22] In species where the volume expansion of the material is significant, it is possible to use nanostructured metals in their place as it reduces the strain and assists in maintaining good cyclability.[23,31]

### 1.2.4 Li-ion Batteries

#### 1.2.4.1 Electrolytes

Early negative electrodes of lithium metal required the use of a non-aqueous electrolyte to prevent hydrogen formation at the anode. Hence, the use of non-aqueous electrolytes was developed alongside both primary and rechargeable battery systems.

The electrolyte used with the earliest lithium metal rechargeable batteries was a $LiClO_4$ salt in a dioxolane electrolyte by Exxon Co which built on work from Stanford university.[22] This system highlighted the importance of a custom electrolyte as the system experienced dendritic growth upon lithium intercalation. Safety issues arise when lithium dendrites deposit at the negative electrode, which can pierce the separator, leading to short-circuiting. The rapid short-circuiting leads to heat generation which can ignite an organic electrolyte.

One strategy to combat this was to use polymer electrolytes. In 1978 Armand *et al.* presented a solvent free solid-state polymer electrolyte which was designed to prevent dendrite formation.[32] Their electrolyte was a complex of a lithium salt and a coordinating polymer (lithium triflate and poly(ethylene oxide)). However, although successful, the presence of lithium metal still made the system too unsafe for commercialisation.

With the phasing out of metallic lithium and the introduction of the intercalation anode, the safety of using organic electrolytes was increased. The common electrolyte used current commercial in Li-ion batteries is $LiPF_6$ dissolved in a mixture of organic solvents such as propylene or ethylene carbonate.[17] Organic solvents lend some of their high ionic conductivity to the cell, allowing for fast charge transfer. Carbonate based solvents are the most prevalent due to their aprotic nature and also their high dielectric current.[17] The presence of ethylene carbonate is crucial in ensuring the reversibility of the cell, as it decomposes quickly during the first charge to form the SEI layer. This rapid degradation minimises the loss in rate of charge transfer and ensures that the cell operates consistently. However, many carbonate species have flash points below 30 °C, hence they are extremely flammable and can explode easily.[33] The practical electrochemical window for alkyl carbonate/$LiPF_6$ electrolyte species is 1.5 V to 5 V vs. Li.[34] The electrolyte decomposes to form LiF and $PF_5$, along with some HF if any protic species are present.

Additives are often added to electrolytes in order t increase their chemical and thermal stability, which can increase the cycle life and performance of the battery.[35] Vinylene carbonate (VC) and lithium bi-oxalatoborate (LiBOB) assist the formation of the passivating SEI layer. Ionic liquids (ILs) are currently being investigated to improve anodic stability. Additives are also being used to increase the operation temperatures of Li-ion systems, such as the addition of

ethyl methyl carbonate (EMC), as a quaternary component to EC-DMC (ethyl carbonate-dimethyl carbonate) lowered the operation window to reach reasonable conductivities at −40 °C.[36]

### 1.2.4.2 Cathode

Rechargeable Li-ion batteries were first produced in the 1970s using a solid host framework of an insertion electrode to accommodate the $Li^+$ ions.[13] These types of cells are known as rocking-chair cells and are composed of two insertion electrodes with the metal ions held as a guest in one of the electrodes depending on the state of the charge.[11,13] The charge transfer agents are $Li^+$ ions which can diffuse within the host network. Ideal Li-ion cathodes operate between 3 - 5 V and their capacities are typically between 100 – 200 mA h $g^{-1}$.[37] Current commercial Li-ion batteries use intercalation electrodes as both the anode and the cathode, typically $LiCoO_2$ and graphite. Common cathode materials for Li-ion batteries can be divided into three groups; layered oxides, spinels, and olivine structures.

Layered oxide compounds such as $LiCoO_2$, $LiNiO_2$, and $LiMnO_2$ have seen a lot of use in Li-ion batteries.[33] These structures have broad classifications resulting from the stacking of $MO_6$ polyhedra with different orientations along the c-axis of the crystal generates polymorphs which allows for two classifications of structure; O (octahedral) and P (prismatic) type structures.[38] The number following the environment description corresponds to the number of transition metal layers stacked within the unit cell. The main two groups of compounds are the O3 (ABCABC), P2 (ABBA), and P3 (ABBCCA) groups. O3 type structures are stable when the ratio of lithium ions to transition metal oxides is low ($Li_{1-x}MO_2$, where x is high) and the average oxidation state of the metal ions is +3. The P2 type structure has a different optimal environment to the O3

type, where the structure is stable with higher quantities of lithium (x = 0.3 – 0.7) and the average oxidation state of the transition metal ion is +3.3.[6]

$LiCoO_2$ is the most widely utilised layered metal-oxide cathode structure, using coke as the anode material and $LiPF_6$ dissolved in propylene carbonate and dimethyl carbonate as the electrolyte.[17] $LiCoO_2$ has alternating layers of monovalent lithium ions and anionic cobalt and oxygen atoms arranged as edge-sharing octahedra. $LiCoO_2$ forms a cubic close packed array where the Co(III) and lithium ions occupy octahedral vacancies in the structure (Figure 2).

However, the reversibility is low and only 0.5 Li per formula unit are capable of inserting, and the cells have a reduced capacity of 150 mA h $g^{-1}$ at 4 V vs. $Li^+/Li^0$.[17] Isostructural compounds such as $LiNiO_2$ and $LiMnO_2$ have been suggested as suitable alternatives. However, the presence of nickel in $LiNiO_2$ causes instability due to lithium site occupation. Stoichiometric ratios of Co and Ni in $LiCo_{1-x}Ni_xO_2$ $(0.1 \leq x \geq 0.3)$ have also been investigated, as well as the introduction of aluminium, iron, and magnesium into the nickel oxide system, $Li(Ni,M)O_2$.[17,39] $LiMnO_2$ suffers from very poor cycling performance as the $Mn^{3+}$ ions will disproportionate in aqueous solutions to other stable oxidation states [40]which leach into the electrolyte reducing the capacity and destabilised the SEI.[37]

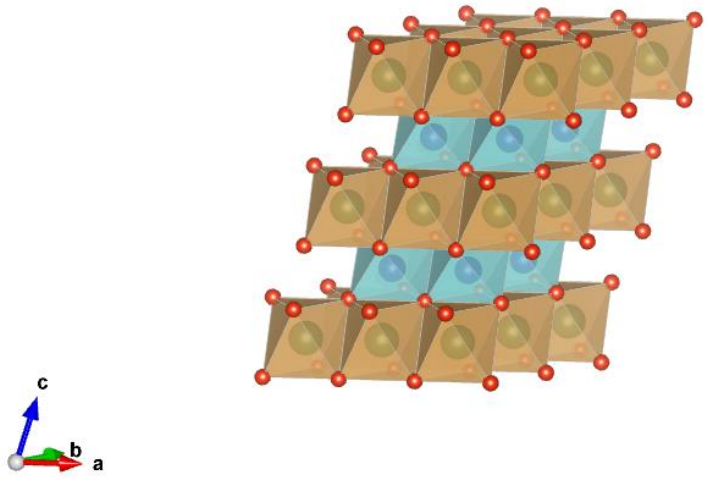


**Figure 2: Crystal structure of $LiCoO_2$ in space group R-3m.**

Spinel-based cathodes are based on layers of $LiMn_2O_4$. This species is readily available and non-toxic. It has a lower reversible capacity of 120 mA h $g^{-1}$ at 3.8 V vs. $Li^+/Li^0$ when compared to $LiCoO_2$. The edge-sharing octahedra produce a very stable internal structure, which can reversibly integrate $Li^+$ without excessive volume expansion.[41] These systems use a ZnO coating or metal doping to avoid the adverse effects of $Mn^{2+}$ leaching.[37]

Olivine structured polyanionic compounds have also been popular as cathode materials. These compounds have the general formula $LiMXO_4$, where M is a transition metal and X is S, P, As, Mo, or W. Polyanionic compounds such as $LiFePO_4$ have high capacities of 170 mA h $g^{-1}$ at an operating voltage of 3.34 V vs. $Li^+/Li^0$. However, the material suffers from low electrical conductivity and low ion diffusion, as the olivine structure can only tolerate one dimensional diffusion.[42,43]

### 1.2.4.3 Anode

Lithium metal anodes offer the lowest redox capacity, thereby maximising the theoretical capacity of the overall cell. Metallic lithium also offers the highest specific capacity of 3860 mA h $g^{-1}$, a standard potential of −3.05 V vs. SHE (standard hydrogen electrode), and a low atomic weight of 6.94 g $mol^{-1}$.[44] This also enables the material to have a charge output of 4 A h per gram of material.[11] Owing to these characteristics it has been commonly used in primary and secondary batteries since the 1970s. However, lithium metal has been proven to be highly unsafe during long-term operation. More specifically, during operation, an inhomogeneous deposition of lithium plating occurs on the anode surface. After many cycles, this plating produces dendritic growths, *i.e.* branches of highly reactive lithium with a large surface area. If the separator in the cell

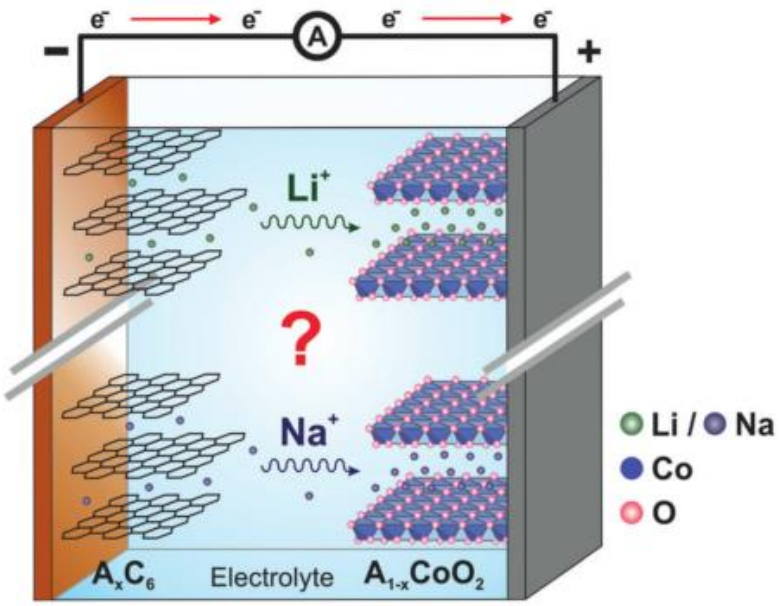


**Figure 3: Schematic comparison of Li- vs Na-ion technology, using a Carbon-based (graphite) anode and $LiCoO_2$ cathode.[45] Reprinted with permission by John Wiley and Sons.**

becomes perforated by the dendrites, the cell can short circuit rapidly generating heat, which can then ignite the organic electrolyte.[11]

To mitigate the disadvantages of using pure lithium metal as the anode it was proposed that a different $Li^+$ insertion electrode could take its place. However, this substitution does lead to a loss in theoretical capacity. To date, the most widely used anode material is graphite and other carbonaceous materials, which are known to possess high capacities. The structure of graphite consists of layers of a honeycomb-type lattice, with interlayer spacings of 0.142 nm. It is this spacing that provides the vacancies required for successful Li-ion diffusion. Highly crystalline graphite provides the most ordered internal structure and has a theoretical capacity of 372 mA h $g^{-1}$. The layers in the graphite allow for charged ions to intercalate into the host structure with ease, a process which is almost fully reversible.[16] The insertion of lithium into graphite can be described by,

$$xLi^+ + xe^- + 6C \leftrightarrow Li_xC_6 \qquad (1.2)$$

where graphite is capable of intercalating 1 lithium atom per 6 carbon atoms. However, graphite does not offer complete reversibility upon cycling. SEI formation and solvated lithium insertion hinder the cyclability and increase cell resistance. For graphite, SEI formation occurs at around 0.2 V and limits the columbic efficiency to 85 - 90%.[13]

In 2000 Tarascon *et al.* demonstrated the potential of conversion electrodes composed of nano-sized transition metal oxides of Co, Ni, Cu, and Fe, with their electrode's capacities of up to 700 mA h $g^{-1}$ with 100% capacity retention after 100 cycles.[18] As a result, it was theorised that the reaction mechanism was centred around the formation and decomposition of $Li_2O$. However, the larger size of the nanoparticles (100 Å – 50 Å) investigated by Tarason *et al.* made the system highly sensitive to aggregation which impeded functionality.[18] Binary species such as metal fluorides, e.g., $FeF_2$ and $CuF_2$ have also been developed which enable ion diffusion through a complex continuous network of metallic nanoparticles. However, as before, the larger nanoparticles hinder recyclability.[19]

Lithium titanium oxide (LTO), $Li_4Ti_5O_{12}$, is an alternative to graphite which possesses a very low volume expansion of 0.2% upon cycling. LTO also possesses a high equilibrium potential allowing operation above 1 V. This reduces the growth of the SEI layer and hence decreases the risk of dendritic growth. Although this material has a high specific capacity of 175 mA h $g^{-1}$ and a long cycle life, the overall capacity and operating voltage are very high which produces Li-ion batteries with low energy densities.[46]

It is also possible to generate anodes by alloying lithium with electrochemically active metallic or semi-metallic elements. The process was first established in the 1970s. In 1986, alloying negative electrode materials of Li-Sn, Li-Sb, and Li-Bi was suggested by Wang *et al.* as an alternative to using metallic lithium negative electrodes. These electrodes were prepared using a propylene

carbonate electrolyte. Although the binary alloys suggested suffer from lower specific energies and energy densities, the prevention of dendritic growth ensured that the electrodes were capable of longer cycle lives when compared to metallic lithium systems.[47] In this study, the lithiation of a Li-Sn alloy at 400 °C produced kinetically influenced one-phase system, corresponding to $Li_5Sn_2$ at high temperatures and $Li_2Sn_5$ at lower temperatures. Similarly, antimony produced two phases, $Li_2Sb$ and $Li_3Sb$, at voltages of 0.956 and 0.948 V, respectively. However, given that the plateaus exist above 0.8 V, it was suggested that they would not make suitable negative electrode materials in lithium-based cells.[47]

The process of alloying involves breaking the bonds between host atoms, thereby inducing large structural changes.[23] As the host structure is broken down, and therefore does not constrain the reaction, alloys have higher theoretical capacities than standard conversion or intercalation materials. For example, Li-Si alloys have a theoretical capacity of 4200 mA h $g^{-1}$, whilst graphite has a theoretical capacity of at 372 mA h $g^{-1}$.[23,48] Alloying materials also benefit from being able to accommodate higher concentrations of charge carrying ions in their host structures, whilst maintaining a low operating potential of below 1.0 V.[49,6]

## 1.3 Sodium-ion Batteries

One of the greatest factors influencing the push for the use of Na-ion batteries is the fact that sodium is naturally abundant, and can be found in salt-water and soda ash (sodium carbonate) deposits, making it highly abundant with 23 million tonnes of soda ash in the United States alone.[50] Also, the lower costs associated with the production of sodium derivatives such as sodium carbonate over lithium carbonate ultimately leads to sodium being a cheaper alternative to Li.[6] For comparison, lithium carbonate is priced at $5000 per ton whilst sodium carbonate precursors are $135-$165 per ton.[50,51]

Sodium is also a sensible chemical substitution for lithium. Both metals are in group 1, with the same valence shell occupancy and are stable in the +1 oxidation state. However, the increased atomic weight and larger ionic radius present issues for direct substitution. Hence, new materials need to be developed to match the performance of current Li-ion batteries.[24]

Although chemically and physically similar, there are some significant differences between the two, which have had a direct impact on the translation of Li research into Na-based cells. $Na^+$ ions are larger than Li (1.02 Å vs. 0.76 Å), which presents obvious issues for insertion materials, as well as to the challenges associated with volume expansion, ion transfer kinetics, *etc*. Sodium is also less energy dense as the element is heavier (23 g $mol^{-1}$) than lithium (6.9 g $mol^{-1}$) with a higher electrode potential (−2.71 vs. −3.02 V, both against a standard hydrogen electrode).[6] This loss of potential is believed to be due to the more diffuse electron shells surrounding the sodium ion. Na ions also typically favour octahedral over tetrahedral coordination and are less polarising than lithium ions. As a result, it affects the species that form during cycling by altering the coordination and

immediate environment surrounding each ion which subsequently affects the crystal structures formed.[45]

Lithium and sodium both pose difficulties as they are highly reactive elements in non-inert atmospheres, however, the real challenge they present is the differing performance of their analogues when in same-system situations. Early research indicated that the standard graphite anode cannot be used with Na. The first successful sodium battery was based on the metallic sodium system using a sulphur positive electrode. This battery operated at ~300 °C with molten electrodes, which is understandably not suitable for mass commercial applications within consumer electronics.[52]

### 1.3.1 Electrolytes

Although a large ionic radius can be a disadvantage when considering ion mobility, in some cases, it can be beneficial. For example, preventing strong solvation of the guest ions into the electrolyte. It has been shown that the $Na^+$ ions in organic solvents have 30% less desolvation energy, meaning that the $Na^+$ ions are more favourably removed from solutions.[45,53] The magnitude of the solvation energy is very important for governing the kinetics of insertion at the electrode-electrolyte interface, as charge transfer depends on the extent of ion solvation in the electrolyte. Lithium ions possess a higher solvation energy barrier than sodium as they have a higher charge density, making them less viable in polar solvents when compared to sodium ions.[38]

Common electrolytes for Na-ion batteries include $NaPF_6$ and $NaClO_4$ in carbonate esters such as propylene carbonate. However, it is noted that metallic sodium will readily corrode when in contact with organic solvents and high dendritic growth at ambient operating temperatures.[50] Highly reducing intercalating anodes may also need further stabilisation to prevent the formation

of species, such as sodium propyl carbonate, via decomposition which may reduce the overall capacity of the system.[50] At present, considerable research is being placed on developing compatible electrolyte/solvent combinations.

### 1.3.2 Cathode Materials

Research on cathodes for Na-ion batteries is focused on intercalation electrode materials, which need to be capable of functioning as a host material with little volume expansion and good cyclability. Calculations comparing the intercalation potentials of cathode materials in $AMO_2$, $AMS_2$, $AMPO_4$, and NASICON *(vide infra)* Na-ion systems vs. those in Li-ion systems (where M is the transition metal *i.e.* iron or manganese and A is Li or Na) indicated that there was a loss of 0.18 – 0.57 V from the intercalation potential and demonstrated the sluggish kinetics of ion diffusion due to the increased weight of sodium.[50,54] Appropriate cathode materials typically possess structures similar to those in Li-ion cathodes. However, it is noted that the limitations of Na-ion kinetics results in environments which typically favour six-coordinate environments (either octahedral or prismatic). As a result, this places some limitation on the structures available due to the ratio between the radii of sodium ions and the interstitial sites. This results in two main categories of cathode materials; polyanionic networks with octahedral interstitial sites and layered transition metal oxides with six-coordinate structures.[50]

Metal oxide-based cathode materials are composed of sheets of edge sharing octahedra with the general formula $Na_{1-x}MO_2$. Discussions of the general formula for metal-oxide cathode materials can be seen in the previous section on Li-ion battery cathode materials (**Error! Reference source not found.**). As with Li-ion batteries, one of the earliest developed cathode materials for Na-ion batteries was the P2-type $Na_xCoO_2$. This species was investigated by Delmas *et*

*al.,* and the P2 structure was stable at compositions of $0.46 \leq x \leq 0.83$.[55] Delmas *et. al.* suggests that the $Na^+$ distribution was responsible for the structural changes during cycling. Sodium- ion diffusion through the structure was observed to be faster than that for lithium ions which was confirmed by Mo *et al.*, with even faster diffusion observed for the O3-type $NaCoO_2$ phase.[56] This has been largely attributed to the larger slab spacing in transition metal oxides.[50,54,57] Mo *et al.* demonstrated the migration of sodium ions through a honeycomb-like internal structure, producing a reversible capacity of 107 mA h $g^{-1}$ between 2 – 3.8 V vs. $Na^+/Na$.[56]

In a similar manner to $Na_xCoO_2$, P2-type $Na_xMnO_2$ exhibits electrochemical activity with a Na composition of $0.45 < x > 0.85$ Na composition. $Na_xMnO_2$ has been shown to be a viable positive electrode material due to non-toxicity and cost effectiveness. However, the reversibility of sodium insertion was poor due to strong Jahn-Teller distortions around the $Mn^{3+}$ ions.[58] This could be mitigated via the substitution of transition metal cations into the structure such as Mg, Ni, and Cu.[59] Kim *et al.* demonstrated that the substitution of lithium and nickel into the structure can deliver a discharge capacity of 95 – 100 mA h $g^{-1}$, with an average of 3.4 V vs. $Na^+/Na$.

Some examples of metal-based oxides are $NaFeO_2$ with trivalent iron ions and Na-Mn-O compounds, the latter having many different phases and polymorphs.[38,60] $NaFeO_2$ has been shown to have with a reversible capacity of 94 mA h $g^{-1}$ at an operating voltage of 3.2 V, demonstrating the efficacy of layered metal oxides as positive electrode materials.

Interestingly, sodium ions can form different insertion materials to lithium, as sodium atoms are able to effectively bond with some species that lithium cannot. For example, Komaba *et al.* demonstrated the electrochemical activity of $NaCrO_2$ as an insertion compound in Na-ion batteries, where $NaCrO_2$

exhibited a reversible capacity of 120 mAh $g^{-1}$ whilst $LiCrO_2$ is inactive in Li-ion batteries.[45,61]

Polyanionic cathodes usually exist as phosphate $(PO_4)^{3-}$, pyrophosphates $(P_2O_7)^{4-}$, fluorosulphates $(SO_3F)^-$, and oxychlorides $(OCl)^{3-}$. Polyanionic compounds have been shown to be more robust and have higher thermal stability than metal oxides due to the presence of strong X-O covalent bonds in the system. Additionally, the inductive effect of the polyanionic groups improves the operating potential against $Na/Na^+$ cells.[62]

Olivine $FePO_4$ was one of the first polyanionic phosphate cathode materials. The structure of this material consists of channels of $FeO_6$ octahedra linked together by $PO_4$ polyhedra, as shown in Figure 4. Synthesised from the delithiation and subsequent sodiation of its lithium analogue, $LiFePO_4$, this compound has a theoretical capacity of 154 mA h $g^{-1}$.[63] The basic structure can be stabilised by partial or full replacement of Fe by other transition metals, and combinations of phosphate and pyrophosphate ions.[38,64] The thermodynamically stable maricite phase of the $NaFePO_4$ structure, which is electrochemically inactive due to a lack of Na diffusion pathways through the structure, can be made active by preparation as nano-sized phases, producing a 142 mA h $g^{-1}$ capacity with 95% cycle retention after 200 cycles.[65] Unfortunately, polyanionic systems can become hydrated easily via water absorption, which is highly detrimental for the battery system.[6] Polyanionics for Na-ion batteries also tend to have lower average voltages than their lithium equivalents. For example, $LiFePO_4$ has a higher operating voltage (3.5 V) when compared to its Na-ion analogue $NaFePO_4$ (3.0 V).[45,64]

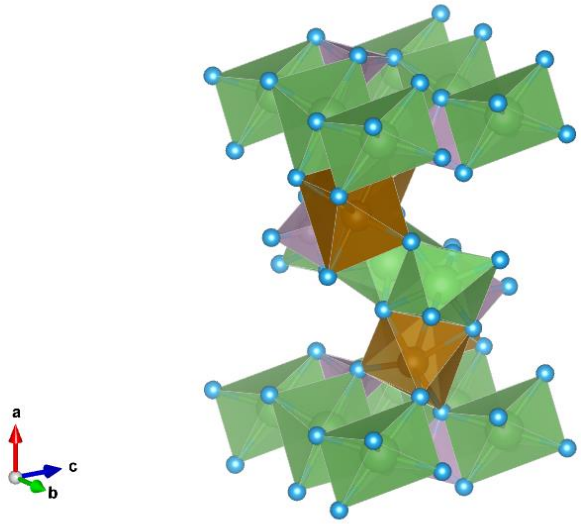


**Figure 4: Crystal structure of olivine $NaFePO_4$ with space group Pnma .**[63]

NASICON (Na Super Ionic Conductor) compounds have also been produced as polyanionic positive electrode materials. NASICON compounds are based on corner sharing $MO_6$ and $XO_4$ polyhedra typically around vanadium redox couples. Their wide open frameworks enable fast ion conduction.[66]

Unfortunately, polyanionic compounds exhibit lower electrical conductivity than metallic oxides and, hence, additives must be used, such as carbonaceous compounds, to improve the electrochemical performance. Kawabe *et al.* used a carbon coated $Na_2FePO_4F/C$ to deliver 110 mA h $g^{-1}$, 75 % capacity retention across 20 cycles.[67,68]

Cathode materials are not limited to solely inorganic materials. It is also possible to synthesise organic-based cathodes, which are typically more environmentally benign and more readily available, as they are free of minor metals. For example, $Na_2C_6O_6$ mimics the layered structure of metal-oxide cathodes and, due to the conjugation of the carbonyl groups, exhibits n-type properties, where the material acts as if it is doped to enhance the conductivity. The bulky internal structure of $Na_2C_6O_6$ makes it ideal to host Na ions The carbonyl groups leads to a reversible capacity of 170 mA h $g^{-1}$ and an average

working voltage of 2.18 vs. $Na^+/Na$.[69] The energy density of this material (370 mWh $g^{-1}$) enables it to perform comparably with inorganic materials for Li-ion batteries and demonstrated it to be a promising cathode for Na-ion batteries.

### 1.3.3 Anode Materials

The development of viable anode materials for Na-ion batteries has presented more problems than the cathode material.[24] This is largely owing to the larger ionic radius of sodium when compared to that of lithium (102 pm vs. 76 pm, respectively). This has obvious and immediate implications on the kinetics of the charge transfer and the mobility of the guest ions within the electrode, as the rate of transfer and current of the system will be reduced.[24] Hence, the insertion electrode material needs to be able to safely accommodate larger ions whilst maintaining cyclability. Research into more robust materials is needed to develop a material that can perform to an equivalent standard for Na-ion batteries. Figure 5 shows a simplified comparison of the three main reaction pathways for electrode materials, this has been included to aid understanding in this section.

In Na-ion batteries the performance of graphite is impeded by electrolyte/electrode degradation in Na-ion batteries.[70,71] Moreover, the voltages achieved in Na-ion batteries using graphite as the anode were sub-optimal and could not compete with the Li analogue.[6] Recent DFT (density functional theory) studies by Nobuhara *et al.* on Na/graphite systems have suggested that this may be due to the stretching of C-C bonds within the graphite sheets, with many $NaC_x$ compounds being unstable.[45,72] An alternative strategy is to use co-intercalation of graphite within a solvation shell (*vide infra*) where the solvation shell of the sodium guest ions is also inserted into the graphite anode.[73] For example, using a digylyme-based electrolyte, Jache and Adelhelm produced a compound of

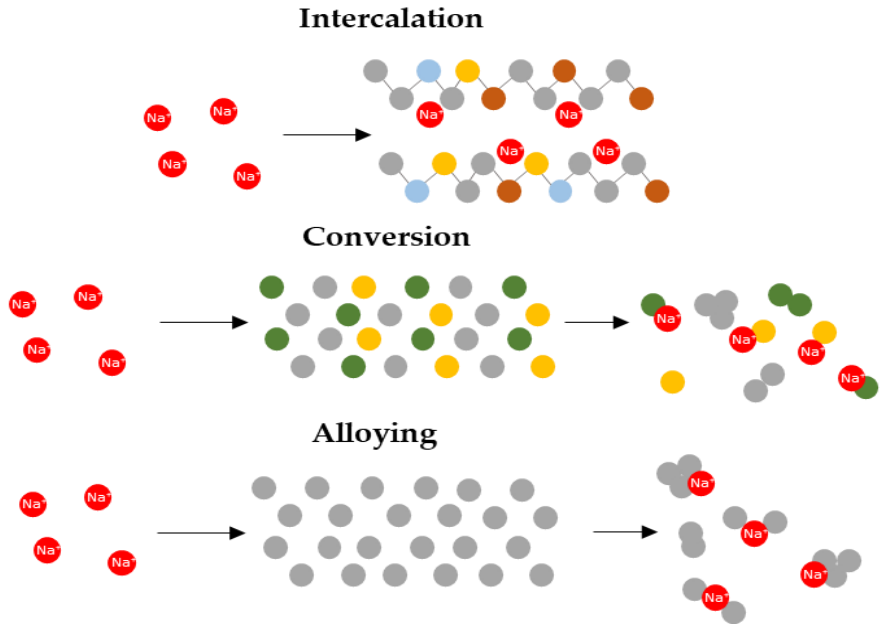


**Figure 5: A simplified comparison of the three main reaction mechanisms for electrode materials. Sodium ions are indicated in red and metallic species are represented in grey; other species are represented by assorted colours.**

$Na(diglyme)_2C_{20}$ with a capacity of 100 mA h $g^{-1}$ over 1000 cycles. Despite the larger size of the solvated sodium ion species the reaction demonstrated very good reaction kinetics and reversibility with very little structure degradation to the graphite layers. This performance is superior to that of the lithium analogues but the overall lower capacity makes it a less favourable option.[45,73]

A distinguishing feature of the anode material is that the electrolyte naturally decomposes at the surface of the electrode. Hence, anode materials therefore need to be able to accommodate the SEI, which can be electronically insulating whilst also remaining permeable for cations and enabling charge transfer.[45] This is one of the many challenges associated with developing useful and functional anode materials. Hence, this is often considered to be more challenging than the development of the cathode counterparts.

Metal oxide compounds have also been shown to provide an alternative solution to negative electrode materials for Na-ion batteries. Compounds such as $Na_2Ti_3O_7$ have low operating voltages (0.3 V) and reversible capacities of 150 mA

h $g^{-1}$ which makes it an excellent anode material.[50,74] In addition to this, it can accommodate two sodium ions per formula unit and was lauded as the lowest-voltage insertion compound for Na-ion batteries. Titanium-based oxides have also been studied the most extensively studied due to their low operating voltage, environmentally benign nature, and low cost.[75,6]

An alternate research direction for negative electrode materials is to pursue a pathway towards electrodes which undergo an alloying mechanism. Sodium is known to undergo alloying reactions with the elements in groups 13, 14, and 15 as well as their compounds (oxides, sulphides, and selenides).[24] For example, species such as Sn, Sb, As, and Ge have been shown to possess high theoretical capacities, e.g., metallic anodes of Sn exhibit a theoretical capacity of 847 mA h $g^{-1}$, forming $Na_{15}Sn_4$.[24,76] It is also possible to alloy sodium to antimony, which can exhibit a capacity of 600 mA h $g^{-1}$ over the course of 160 cycles. Due to this, there has been more research and industry focus on alloying based compounds.[45,77]

In comparison to the performance observed for conversion electrodes, the sodiation of alloying compounds is a complex step-wise process with the formation of a mixture of amorphous and crystalline phases. This is strongly influenced by the experimental conditions. Hence, understanding the chemical reactions involved in alloying reactions can be extremely challenging. The use of pure metal anodes such as Sn has a relatively high specific capacity 847 mAh $g^{-1}$, however it undergoes a volume expansion of 420% upon cycling to completion, culminating in the formation of $Na_{15}Sn_4$.[24,78] This structural formula determines that one Sn atom is capable of accommodating 3.75 Na atoms.[75,79] Sb, has a lower volume expansion (390%) but also a lower theoretical capacity of 660 mAh $g^{-1}$. [80,77,81] The sodiation of Sb proceeds via two major steps; the first involves the formation of amorphous $Na_xSb$ which then forms two separate cubic and

hexagonal crystal structures. Both hexagonal and amorphous Sb electrodes were structurally sound across repeated cycles.[24,82]

However, the alloying of compounds to sodium has many challenges, which need to be tackled in order for their use to become wide-spread. Alloy-based anodes undergo rapid capacity fade upon repeated cycling due to a combination of the volume expansion and SEI formation (see 1.2.3.1) which cause direct loss of electrical contact, and aggregation of metallic nanoparticles which slows the charge transfer kinetics. One way reduce volume expansion of the electrode upon sodium insertion is to introduce a carbonaceous-metal nanocomposite where metallic nanoparticles can be dispersed within the carbon network. The carbon host network can mitigate the volume change of the Sn nanoparticles and prevent aggregation. However, this method reduces the active metallic material present in the electrode thereby limiting the capacity as less sodium can be stored in the electrode during cycling.[24]

Sb based carbon-nanocomposites (Sb-C[15], and SbSn-C[16]) have demonstrated interesting performances with reversible characteristics of between 50-600 mAh $g^{-1}$ over many cycles according to Darwiche *et. al*.[77] Upon investigation of the reaction mechanism, Na/Sb was found to undergo a more complex mechanism than it's Li/Sb counterpart producing unusual amorphous intermediate phases. The better cycling performance has been connected to a lower volume expansion of from the transition of Sb to hexagonal $Na_3Sb$ (55.9 $Å^3$) compared to $Li_3Sb$.[77] The formation of the amorphous phase has also been suggested to relieve strain on the system resulting in improved cycling.

### 1.3.3.1 Binary alloys as Conversion Anode Materials

Alloying electrochemically active materials together is one of the fastest growing areas of research for anode materials. The combination of elements that are active to the species being inserted (*e.g.*, Li, Na, etc) often results in electrochemical behaviour that differs from that of the individual parent materials. One of the most important impacts of these materials is that they undergo conversion reactions upon sodiation. Typically, the binary alloys contain small grain areas of each active material in order to reduce the likelihood of multiple phases being produced during cycling.[22]

Binary alloys can be classified as either active/active (where both species are electrochemically active), or active/inactive (where only one of the species is electrochemically active). Typically, the primary role of alloys is to improve the cycling performance whilst buffering any volume expansion.[6]

Combining an active material to an inactive material is introduced in order to alter the operating voltage and grain size, as well as reducing any associated volume expansion. An additional advantage of using active/inactive alloyed elements is increased smoothness and simplicity in the cycling pathway. In cases where the active material exists in small nanosized grains within an inactive matrix, larger single phase regions are more common with fewer instances of multi-phase regions which makes the cycling pathway of the material less complex and often improves cell performance.[22,83]

The alloying of Sn to another active material has seen significant improvement over pure Sn. For example, by alloying Sn and Sb, tuning of the redox process has been observed which is capable of enhancing the cycle life of the system. This is believed to be due to the stabilisation of the microstructure of the crystal in comparison to either of the pure metals.[45] SnSb has been shown to

be stable across 100 cycles with a capacity of 500 mAh $g^{-1}$ which makes it an excellent candidate as a new negative electrode material. The mechanisms involved in with the interaction of Li with SnSb assist in maintaining the structure of the electrode, thereby reducing the impact of volume expansion, and suppressing Sn aggregation, which ultimately increases the surface area of active material, thereby improving cycling performance.[22,84]

Binary alloys have also been developed using carbon as an electronic conductivity enhancer and refined nanoscale regions of SnSb. These compounds proceed first by the single-phase reaction of Sb with Na to form $Na_3Sb$ followed by alloying to Sn. In this binary alloy, both of the metals are electrochemically active and participate equally in the electrochemical process.[50,85] Xiao *et al.* demonstrated that this system was capable of producing a reversible capacity of 500 mA h $g^{-1}$. The electrochemical profiles they produced show three key features. A plateau at 0.6 V demonstrates the formation of the SEI layer. Further plateaus correspond to the formation of $Na_3Sb$, phases of metallic Sn, and $Na_{3.75}Sn$. The final key feature shows the insertion of Na-ions into a form of carbon called Super P carbon which is a highly conductive form of carbon black.[85] However, the use of graphite can lead to irreversible capacity loss after the first cycle and consequently the cell performance is reduced.[6]

The addition of an inactive third element often mitigates some of the volume expansion of alloying materials.[22] One example studied was a $Sn_xSb$-Ni which when studied as a microcomposite exhibited a capacity of 350 mAh $g^{-1}$ across 150 cycles. Similar behaviour has also been exhibited in SnSb-Zn and SnSb-Cu species.[86,87]

### 1.3.3.2 TiSnSb

TiSnSb is the only ternary alloy of the Ti-Sn-Sb system and has been studied largely in the context of Li-ion systems rather than sodium-ion systems. The structure of the TiSnSb follows a $CuMg_2$ type structure; orthorhombic Fddd symmetry, which possess a rhombic dipyramidal shape similar to that of the olivine and aragonite structures.[88] In this structure the Ti atoms are located in square antiprisms of Sn and Sb atoms, with the Sn atoms occupying the 16f sites, and the Ti and Sb atoms are located on the 16g sites.[87,88] A model of the structure can be seen in Figure 6. The synthesis of TiSnSb was reported by Sougrati *et. al.* in 2011. >90% Ti, Sn, and Sb powders were ball milled under Argon for between 10 to 30 hours.[87]

Titanium as an element is credited with increasing the mechanical resistance of the electrode to volume changes as well as maintaining cycling stability.[87] Marino *et. al.* have demonstrated that during cycling TiSnSb is capable of taking up 5 lithium atoms per formula unit, indicative of a very high theoretical capacity (more than 550 mAh $g^{-1}$) in a Li-ion battery.[86] TiSnSb was shown to undergo a conversion reaction, leading to the formation of Li-Sb and

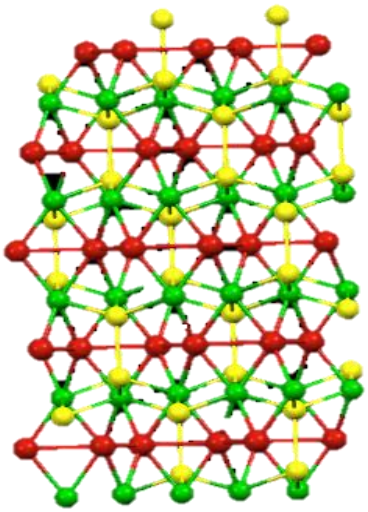

**Figure 6: Crystal structure of TiSnSb with space group Fddd.**[89]

Li-Sn intermetallic compounds.[86] In terms of consistency across multiple cycles, the Li-ion TiSnSb system performed reliably for 50 cycles at a 2C rate. Through studying the electrochemical performance of the alloy, it was reported that there was a simultaneous reaction of Sn and Sb with Li during the first discharge with no preferential reaction indicated.[87] At the end of the first discharge $Li_3Sb$ and $Li_7Sn_2$ phases were produced, phases which were the same as were produced by the Ti/Sn/Sb composite electrodes.[87,90] However, the phases identified in the charge electrode were different with no evidence of metallic Sb or Sn.[87] Although sharing similar discharge phases, in contrast to the performance of the Ti/Sn/Sb composite, the capacity of TiSnSb was found to fade less rapidly.[87] It is important to understand that the rate of charge has a significant impact on the phases formed with a faster charge rate i.e., 4C driving kinetic reactions. Hence although the system has been studied there is still scope for further investigation.

Further investigation of TiSnSb was conducted by Johnston *et. al.* where the relaxation of a lithium TiSnSb system was studied in order to ascertain the reaction mechanism.[90] They studied the material *ex situ* using $^7$Li MAS NMR at a cycling rate of C/2 and 4C. They observed instability in the phases formed at the end of lithiation with large variations in stoichiometry. They tentatively assigned the conversion of TiSnSb into lithium stannide species ($Li_7Sn_2$ or $Li_7Sn_3$), lithium antimonides ($Li_3Sb$), and titanium metal nanoparticles.[90] They found that the instability of the lithiated species led to rapid evolution after discharge as the cell was left to relax.

Further investigations into the cause of the materials excellent cycling ability were attributed to either the presence of the inactive Ti or to the structure of the electrode itself, a structure which they claimed allowed for both the capacity retention and the rate of cyclability. To elucidate whether the presence

of Ti within the electrode was responsible for the good performance of TiSnSb studies were conducted comparing composites of Ti/Sn/Sb to the TiSnSb alloy. The composites used in this experiment were obtained by ball milling Ti, Sn, and Sb powders to various extents. The TiSnSb alloy produced phases of $Li_3Sb$, $Li_xSn$, and Ti. Through X-ray diffraction (XRD) and $^7Li$ NMR it was concluded that the performance of TiSnSb as an alloy is related to intrinsic parameters, which were not fully elucidated in this study. The work of Johnston *et. al.* also supports the conclusion that the addition of Ti through intimate nanoscale mixing helps the reformation of TiSnSb during cycling ensuring reversibility.[90]

## 1.4 Project Aims

The primary aim of this research is to investigate the behaviour of TiSnSb as a ternary negative electrode material for sodium-ion batteries. The behaviour of TiSnSb in a Na-based cell will be analysed via electrochemical discharge and charge profiles of the cells at various rates and the resulting system will be examined using solid-state $^{23}Na$ MAS NMR. TiSnSb will be studied at C/2 and 4C rates at various stages of the charge cycles, focusing on the end of de-sodiation (discharge) and sodiation (charge) in particular.

Initially, research will focus on whether or not successful systems can be created using this material, building on the research already established for TiSnSb with Li-ion systems. The work will also examine the reaction mechanisms undergone by the electrode upon sodiation and de-sodiation.

The addition of titanium to SnSb is expected to help mitigate some volume expansion to ensure cyclability as was observed by Sougrati *et. al.* and Johnston *et. al.* and we should expect to see better performance for TiSnSb than was observed for SnSb.[87] Monitoring the system at different charge rates will

hopefully provide insights into the reaction mechanism in play and explore the impact that kinetic influences have on the system.

It is expected that TiSnSb in a sodium system will produce similar phases to its lithium counterpart so we will expect to see evidence of $Na_xSn$, $Na_xSnb$ in the $^{23}Na$ MAS NMR spectra with the existence of Ti metallic nanoparticles also being hypothesised as was observed by Johnston *et. al.*[90]

# Chapter 2 Experimental Techniques

## 2.1 Sample Preparation

The TiSnSb electrodes used in this research project were synthesised by the Monconduit Group at the Insitut Charles Gerhardt Montpellier, Université Montpellier. The active material was synthesised via mechanical milling of Ti, Sn, and Sb powders under an Ar atmosphere using a SPEX 8000 ball mill. The importance of nanostructuring in conversion materials is well reported within the literature and, in the case of TiSnSb, an active milling time of 24 hours is known to produce the smallest particle size of the TiSnSb alloy.[87]

The Ti+Sn+Sb electrodes were also synthesised by the Monconduit Group at the Insitut Charles Gerhardt Montpellier, Université Montpellier. The active material was synthesised via intimate mixing of Ti/Sn/Sb in a 1/1/1 composition by a short grinding in a pestle and mortar (15 min).[87]

## 2.2 Electrode Preparation

Electrodes were prepared using carboxymethyl cellulose (CMC) as a binder in conjunction with two conductive additives to make the electrode: vapour-grown carbon fibres (VGCB) and carbon black Y50A. The active material and additives were manually ground in a weight ratio of 70:12:9:9 (Active Material/CMC/VGCB/Y50A), mixed with deionised water and milled to form a slurry, which was tape cast onto 22 μm thick copper coil at a thickness of 150 μm. Finally, the electrodes were then dried under vacuum.[90]

## 2.3 Electrochemical Cell Construction

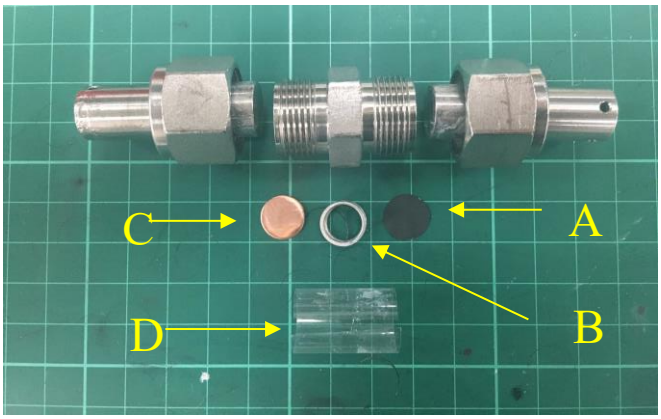


**Figure 7: A breakdown of the components of the Swagelok™-type cell; including (a) the TiSnSb electrode, (b) a spring, (c) the copper disc used as a scaffold for lithium, and (d) a plastic cell liner.**

All electrochemical cells consist of two electrodes, an anode and a cathode, connected via an electrolyte with a glass microfiber separator acting as a physical barrier between the electrodes. Swagelok™ cells were used for the electrochemical cycling of TiSnSb electrodes, and are shown in Figure 7. All cell components were dried overnight in a vacuum oven before being transferred into an Ar-filled glovebox. Due to the air-sensitive nature of the electrolyte, the active material and the metal used as the counter electrode, all cell construction took place inside the glovebox.

## 2.4 Electrochemical Cycling

All electrodes were cycled against sodium metal with 1 M anhydrous $NaPF_6$ (98%, Sigma Aldrich), in propylene carbonate (99.7 %, Sigma Aldrich) (PC) as the electrolyte using conventional two-electrode

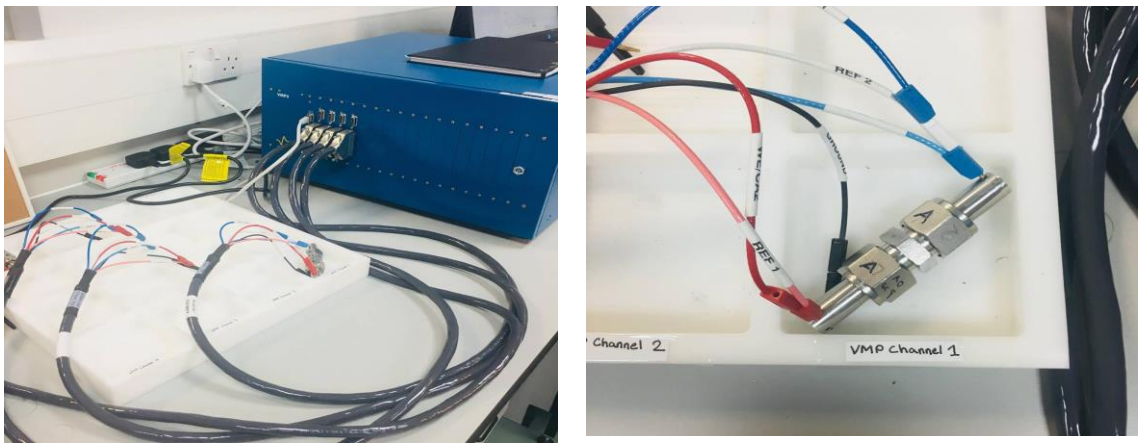


**Figure 8: Left - VMP3 multi-channel potentiostat, Right - Connected TiSnSb cell.**

Swagelok™ cells. Electrochemical discharge profiles were recorded on a VMP3 multi-channel potentiostat from Bio-logic Science Instruments. The cells were cycled under galvanostatic conditions using rates of C/2 (0.5 Na ions per formula unit per hour) and 4C. With a potential minimum of 10 mV and a maximum of 2.5 V, with data points recorded every 5 mV. C rate is defined as the number of sodium ions inserted per formula unit of TiSnSb per hour,*.i.e.,* C/2 is 0.5 Na ions per formula unit of TiSnSb per hour. The cells are then held at a voltage of 0.01 V to prevent relaxation of the system before $^{23}$Na MAS NMR can be conducted.

After cycling, each cell was disassembled in the glovebox, where the active material was extracted, washed with dimethyl carbonate (anhydrous, ≥ 99%, Sigma Aldrich) (DMC) and dried under vacuum for 2 hours using a Büchi drying oven. Samples were then packed into 4 mm zirconium rotors for analysis. Owing to small sample volumes, Bruker Kel-F disposable inserts were used to ensure the sample was in the centre of the rotor.

## 2.5 Solid-State NMR Spectroscopy [90–92]

### 2.5.1 Introduction

Nuclear magnetic resonance (NMR) spectroscopy is a non-destructive analytical technique that can be used to gain an understanding of the molecular-level structure and dynamical behaviours within a system. Almost all elements in the periodic table possess a spin-active nuclide which can be studied using NMR spectroscopy. Hence there are many potential applications. Moreover, NMR spectroscopy can be applied to amorphous, semi-crystalline, and crystalline compounds, as there is no requirement for long-range ordering within the sample.

### 2.5.2 Principles of NMR

Nuclei possess intrinsic angular momentum, **I**, with a corresponding spin quantum number, ***I.*** The spin of a nucleus is determined by the number of unpaired protons and neutrons within the nucleus. The angular momentum of a spin-I nucleus has 2I+1 projections onto an arbitrarily chosen axis, typically z, where the z component of **I**, $I_z$, is,

$$I_z = m_I \hbar \tag{2.1}$$

where $m_I$ is the magnetic quantum number with values ranging from −I to +I, resulting in 2I+1 states that are degenerate in energy. The circulating charge creates a magnetic dipole moment, $\boldsymbol{\mu}$,

$$\mu = \gamma I \tag{2.2}$$

where $\gamma$ is the gyromagnetic ratio of the nucleus. The orientation of $\boldsymbol{\mu}$ is either parallel $(+\gamma)$ or anti-parallel $(-\gamma)$ to **I.**

In the absence of an external magnetic field, all orientations of **I** have equal energy and no central axis of quantisation, meaning they are randomly orientated. This degeneracy is removed upon the application of a strong magnetic field, $\mathbf{B}_0$, and when the field is applied along z, the energy is given by,

$$E = \omega_0 m_I \hbar \mathrm{B}_0 \quad (2.3)$$

When the field is applied along the z-axis the energy is given by

$$E = -\mu_Z \mathrm{B}_0 \quad (2.4)$$

where $\mu_Z$ is the projection of the magnetic dipole moment onto the z-axis and $B_0$ is the applied magnetic field in this direction. This is known as the Zeeman interaction shown in Figure 9.

At thermal equilibrium there will be a slight excess of spins in the lower energy level, giving rise to a net or bulk magnetisation vector, $M_0$. In NMR spectroscopy, in order for a transition to be observable, it must obey the selection rule ΔmI = + 1 and the frequency of any transition given by,

$$\omega_0 = -\gamma \mathrm{B}_0 \quad (2.5)$$

where $\omega_0$ is the Larmor frequency, given in rad $s^{-1}$.

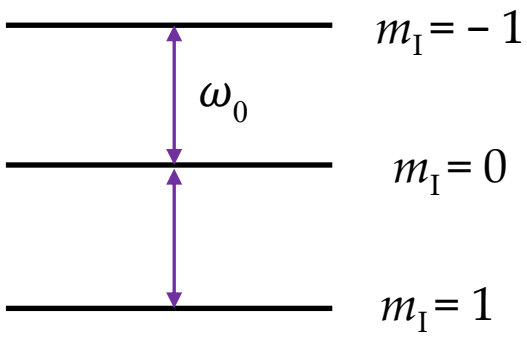


**Figure 9: The effect of the Zeeman interaction upon the nuclear energy levels for spin I = 1.**

### 2.5.3 The Vector Model, Relaxation, and Fourier Transformation

Modern NMR spectrometers employ pulsed NMR methods, in which short pulses of intense rf radiation are applied to a sample. In order for the spins in a sample to be effectively excited, the frequency of this radiation, $\omega_{rf}$, needs to be close to the resonance frequency, $\omega_0$, of the nucleus under investigation. The pulse applied, with strength $B_1$ and duration $\tau_p$, interacts with the nuclear spins in the sample, exciting all resonances simultaneously. As a result, the orientation of $M_0$ is affected. The effect of a pulse is to tilt $M_0$ away from $B_0$ (i.e., the z axis). Once this motion starts, $M_0$ will begin to precess about $B_0$ at the Larmor frequency, $\omega_0$. This process is extremely challenging to visualise, hence a 'rotating frame' is used; a frame of reference which itself is rotating about the z axis at frequency $\omega_{rf}$. In this frame, $M_0$ now precesses around $B_0$ at frequency $\Omega$, with an effective magnetic field $B_0^{eff}$ along the z axis.

In this rotating frame, a pulse can be described as a static field, $B_1$, applied perpendicular to $B_0$. If applied along x, $M_0$ nutates into the xy plane. Once the pulse is removed, $M_0$ undergoes free precession at frequency $\Omega$, given by,

$$\Omega = \omega_0 - \omega_{rf} \qquad (2.6)$$

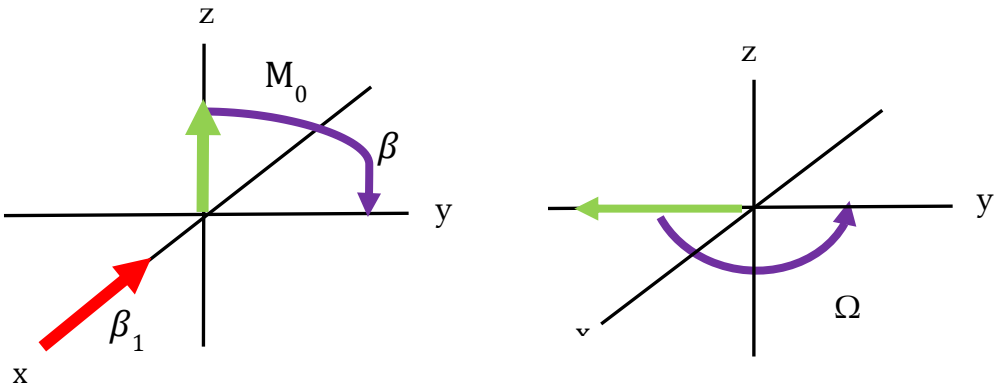


**Figure 10: A) Vector model representation of the effect of a pulse applied along the x axis of the rotating frame on the bulk magnetisation vector $M_0$. B) After rotation into the yx plane the vector undergoes free precession at frequency Ω.**

The 'flip angle' through which the magnetisation nutates is given by $\beta = -\gamma B_1 \tau_p$. In NMR experiments, flip angles of $\beta = 90°$ and 180° are most commonly used.

After a pulse is applied, the system undergoes various relaxation processes, returning it to thermal equilibrium and restoring the Boltzmann distribution. There are two main relaxation effects that dampen the precession of the magnetisation around the z axis; longitudinal or spin-lattice ($T_1$) and transverse or spin-spin ($T_2$) relaxation effects. Spin-lattice relaxation describes the return of the z-component of the magnetisation to equilibrium. Spin-spin relaxation describes the loss of magnetisation from the xy plane and occurs through the interaction between spins. The damped precession of $M_0$ is known as the free induction decay (FID) and is the signal detected in a NMR experiment. The FID is a time-domain signal that requires converting into a frequency-based spectrum. To do this, a mathematical transformation known as a Fourier transformation (FT) is required.

### 2.5.4 Nuclear Interactions

In reality, the field experiences by a nuclear spin is not solely that of the applied magnetic field, $B_0$. In a magnetic field, the electrons around a nucleus circulate, generating a small magnetic field, $B_{int}$, creating two different types of electrical current. Diamagnetic currents oppose the field, thereby increasing the shielding of a nucleus, whilst a paramagnetic current which augments the field, thereby reducing the shielding and making the nucleus more deshielded. The local electron distributions therefore affect the resonance frequency of a nucleus. This produces a new resonance frequency,

$$\omega = -\gamma B_0(1-\sigma) \tag{2.7}$$

where $\sigma$ is the shielding constant. When reporting spectral data, the shielding constant is an inconvenient measure of the chemical shift. Therefore, a deshielding parameter, $\delta$, is used, given by

$$\delta = 10^6\left(\frac{\omega-\omega_{ref}}{\omega_{ref}}\right) \tag{2.8}$$

where $\omega$ and $\omega_{ref}$ are the resonance frequencies of the nucleus of interest and a standard or reference.

#### 2.5.4.1 Chemical Shift Anisotropy (CSA)

In actuality, the shielding of a nucleus is orientally-dependant (chemical shift anisotropy, CSA). In solution-state NMR, the shielding is average to its isotropic value owing to rapid molecular tumbling. In the solid state, however, both the anisotropic and isotropic component of the interactions are present, leading to broadened lineshapes. The CSA can be described as an elongated ellipsoid using the parameters $\sigma_{iso}$, $\Delta\sigma$CS, and $\eta$CS, relating to the isotropic shielding, the shielding anisotropy and the shielding asymmetry, respectively.

Each of these can be used to describe the magnitude and shape of the interaction. As with all orientation-dependant interactions in solid-state NMR, the CSA contains the expression $3\cos^2\theta-1$, indicating an angular dependence.

In polycrystalline samples different crystallites will have different orientations with respect to $B_0$. Hence, the shielding will be different depending on the angle. The distribution of many different lines in a spectrum, each on relating to the orientation of a different crystallite, produces a complex powder pattern.

### 2.5.4.2 Scalar and Dipolar Coupling

Scalar couplings are most prevalent in solution state NMR and arise from the intramolecular through-bond interaction via indirect spin-spin coupling. The coupling provides information regarding molecular-connectivity and molecular conformation. Scalar couplings describe the coupling between NMR-active nuclei. In solid-state NMR the magnitudes of scalar couplings are typically lower than those of the other interactions present in the solid-state, e.g., the quadrupolar interaction. As a result, they are often lost under very broad resonances. Hence, multiplet splitting patterns are relatively rare.

Dipolar couplings are through-space interactions that arise from the interaction between the localised magnetic fields, of nuclear dipoles, $\mu$, that are close in space. Like the CSA, dipolar interactions are orientally-dependant and exhibit an angular dependence proportional to $3\cos^2\theta-1$. Hence, in solution-state NMR they are averaged to their isotropic value owing to rapid molecular tumbling. Dipolar interactions can be both homonuclear and heteronuclear and the magnitude of the interaction is dependent on both the internuclear distance between the two spins and the angle between the internuclear vector and the applied magnetic field. The dipolar interaction can be described by the following,

where $\omega_D$ is the dipolar splitting parameter and $\omega_D^{PAS}$ is given by,

$$\omega_D = \omega_D^{PAS} (3cos^2\theta_{jk} - 1)/2 \quad (2.9)$$

$$\omega_D^{PAS} = \frac{-\mu_0 \gamma_I \gamma_S \hbar}{4\pi\, r_{IS}^3} \quad (2.10)$$

where $r_{IS}$ is the internuclear distances between two spins I and S.

In powdered samples, it is extremely rare to find two isolated spins. Hence, in reality, solid-state NMR lineshapes are broadened due to the interaction of many different dipolar interactions.

### 2.5.4.3 Quadrupolar Interactions

For nuclei with a spin quantum number of I > 1/2 a non-spherical distribution of charge exists around the nucleus, producing a nuclear electric quadrupole moment, eQ. This quadrupole interacts with the electric field gradient, EFG, that is generated at the nucleus because of other atoms present in the system, producing an interaction known as the quadrupolar interaction. This interaction is orientationally dependant and the magnitude of the interaction can be given, in Hz, by the quadrupolar coupling constant, $C_Q$.

$$C_Q = \frac{e^2 qQ}{h} \quad (3.11)$$

For simplicity, the quadrupolar interaction can be described as an elongated ellipsoid with the three principal components of the ellipsoid being described by $V_{xx}$, $V_{yy}$, and $V_{zz}$. In this context, the shape of the cross-section of the ellipsoid can be described by an asymmetry parameter, $\eta_Q$, given by,

$$\eta_Q = \frac{(V_{xx} - V_{yy})}{V_{zz}} \quad (3.12)$$

For values of $0 < \eta_Q < 1$.

The magnitude of the coupling constant often infers useful structural information. For example, cubic and high symmetry systems (e.g., octahedral

and tetrahedral environments) typically exhibit very low values of $C_Q$, owing to the very symmetrical nature of the EFG. In contrast, when systems deviate from ideal symmetry, their value of $C_Q$ can increase substantially.

### 2.5.5 Magic Angle Spinning (MAS) NMR Experiments

Magic angle spinning, of MAS, is a method used for suppressing orientationally-dependant interactions such as the CSA and dipolar interaction. This experiment involves rapidly spinning the sample around the magic angle (54.736°) relative to the external magnetic field. All of the anisotropic interactions discussed thus far possess an orientation dependence proportional to $3\cos^2\theta - 1$ and when $\theta = 54.736°$ these interactions can be reduced to their isotropic value. To successfully suppress the interactions, the spinning speed must be greater than or equal to the magnitude of the interaction being removed.

If, however, the spinning speed is not sufficiently fast, the averaging will be inefficient, and the spectrum will be an envelope of spinning sidebands that are separated by the spinning speed.

MAS is capable of averaging CSA and heteronuclear dipolar couplings that are typically on the order of a few kHz. Quadrupolar and homonuclear dipolar couplings are, however, considerably more challenging to remove, as their magnitudes are typically greater than current commercial spinning speeds.

### 2.5.6 Experimental Procedure

All solid-state NMR spectra were acquired using a Bruker 500 Avance III spectrometer, equipped with an 11.7 T magnet, using a Larmor frequency of 132.3 MHz for $^{23}$Na ($I$ = 3/2). A MAS rate of 10 KHz was used for all $^{23}$Na NMR experiments and chemical shifts were referenced to 1 M NaCl (aq) 0.0 ppm. $^{23}$Na MAS NMR spectra were acquired using a single-pulse experiment with a pulse

length of 1.55 μs and a recycle delay of 5 s, after optimisation. Spectral analysis and fitting were performed using the solid lineshape analysis (SOLA) tool in the Topspin software package.

### 2.5.7 Spectral Analysis

Deconvolution of NMR spectra is carried out by mathematically fitting one or more resonances beneath the overall NMR spectrum. This deconvolution was carried out by simulating Na environments based on published literature.

The shape and intensities of the resonances can be adjusted by altering parameters such as the chemical shift of the resonance. In SOLA, a least squares fitting can then be initiated that solves for the optimum parameters which best fit the observed spectrum. This provides information about the chemical species present.

# Chapter 3 Results and Discussion

## 3.1 Behaviour at the end of the first discharge for TiSnSb

In order to examine the behaviour of TiSnSb it is necessary to run experiments at varying rates of discharge/charge. Initial experiments were run at C/2 and 4C to examine the state of the electrode at the end of the first discharge and first charge. This will provide insights into the formative electrochemical reactions occurring in the system. There have been no previous studies of TiSnSb in a Na system so comparisons must be made to the lithium system studied by *Johnston et al* and to the antimony system studied by *Allen et al.*[80,90]

A sample of TiSnSb was discharged to a cut-off potential of 10 mV at a rate of C/2. The corresponding discharge profile is shown in Figure 11. During discharge, a rapid decrease in potential from an open circuit voltage (OCV) of 2.6 V to 0.8 V is observed, assigned to the formation of the solid-electrolyte interphase (SEI). In general, the potential profile exhibits a progressive decrease that is characteristic of the ternary alloy TiSnSb.[87,93] Based on the electrochemical data presented and the gradual decrease in potential observed, *i.e.*, the lack of any distinct plateau's associated with each of the elements present, it is believed that no distinct or separate electrochemical processes are observed for the sodiation of tin or antimony, implying that TiSnSb proceeds via a conversion mechanism. This is in good agreement with discharge profiles previously reported for electrodes which are known to undergo conversion reactions.[87]

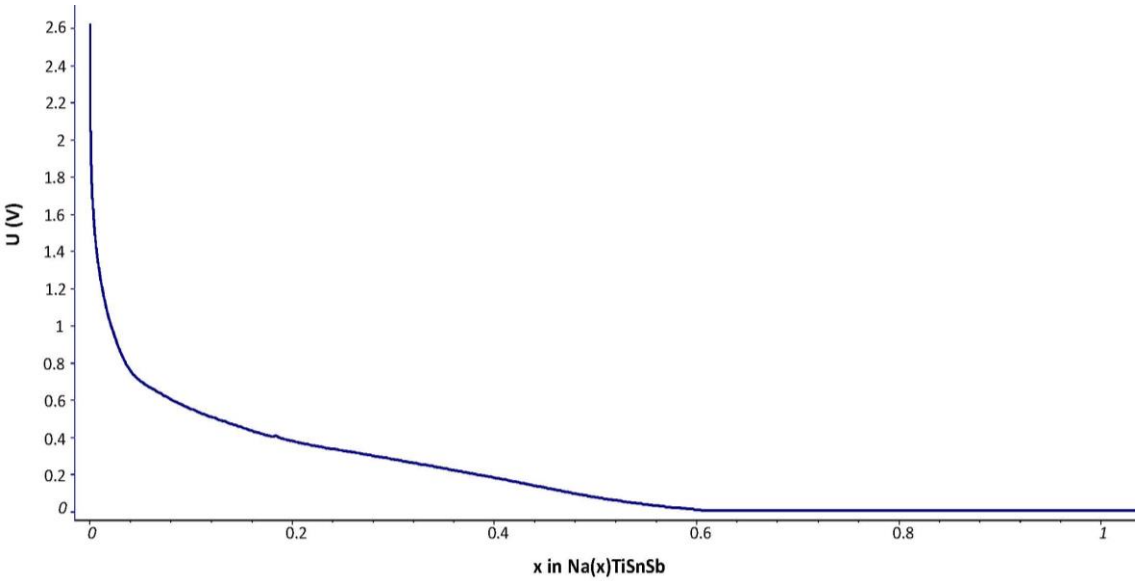


**Figure 11: The potential profile obtained for TiSnSb at the end of the first discharge against sodium. The sample was cycled at a rate of C/2.**

At the end of discharge, approximately 0.6 Na per formula unit are inserted into the TiSnSb structure. This is considerably lower than the number of Li ions that can be inserted into TiSnSb. This is likely attributed to the size of Na when compared to lithium.[87,94] During discharge, sodium is inserted into the TiSnSb structure via a conversion mechanism. Hence, when the Na is inserted, the original TiSnSb structure is believed to 'breakdown' producing a series of sodiated Sb and Sn phases. Based on previous XRD studies and the electrochemical data presented this is believed to happen here. Research by Sougrati *et. al.* conducted *in situ operando* XRD on ball-milled samples of TiSnSb against lithium observed a destruction of the host TiSnSb structure to produce cubic β-$Li_3Sb$.[87] Through $^{119}Sn$ Mössbauer studies of the same system it was determined that series of Sn rich Li-Sn intermetallic compounds were formed throughout discharge such as LiSn and $Li_7Sn_3$.[87]

In order to investigate the phases formed at the end of discharge, $^{23}Na$ solid-state NMR experiments were completed. At the end of discharge, the cell

was stopped, disassembled and the active materials were extracted, rinsed and dried prior to acquisition of the $^{23}$Na MAS NMR spectra. The corresponding $^{23}$Na MAS NMR spectrum obtained at the end of the first discharge is shown in Figure 12.

The spectrum obtained displays a single relatively broad resonance at δ = 9.1 ppm. Both Sn and Sb are chemically reactive to Na, hence, the resonance observed likely contains multiple overlapped Na sites corresponding to sodiated Sb and Sn phases formed. From XRD it is known that the phases $Na_{1-x}Sn_x$ and $Na_{1-x}Sb_x$ form at the end of sodiation. Hence, these ae likely to be present in the NMR spectrum. Using the solid line shape analysis (SOLA) fitting program in the Topspin software program, the resonance was fitted using two distinct sodium environments, as seen in table 1. The quadrupolar parameters ($C_Q$ and $\eta_Q$) obtained for each site are also given in Table 1.

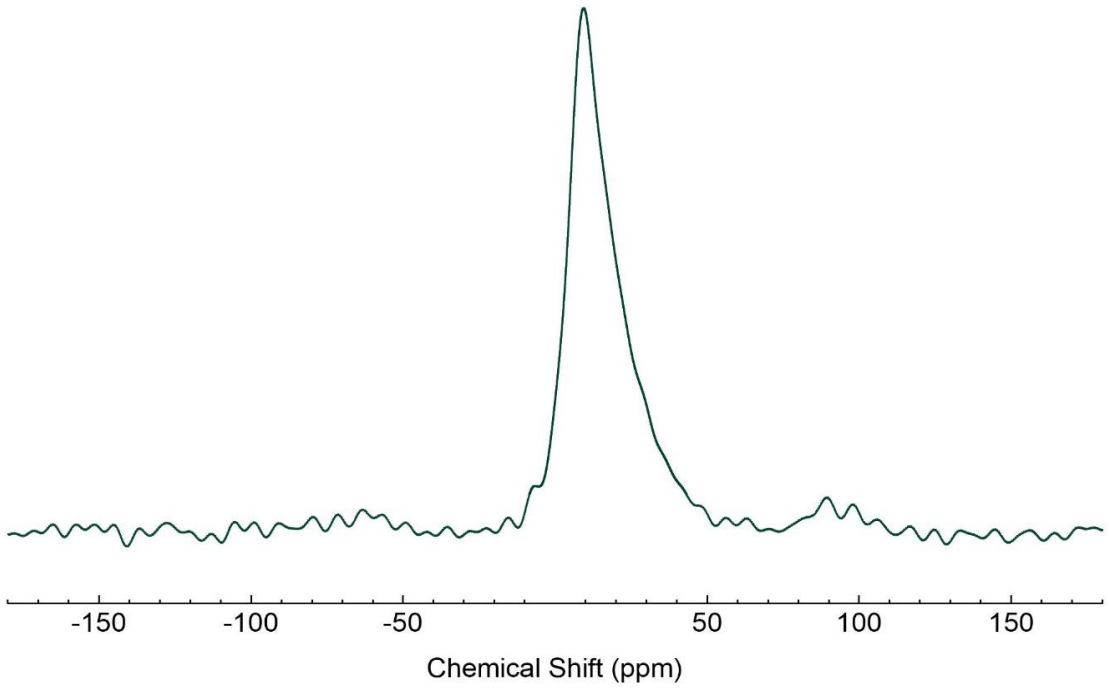


**Figure 12: The $^{23}$Na MAS NMR spectrum obtained at the end of the first discharge (sodiation) of TiSnSb. The sample was cycled at a rate of C/2 and the MAS rate was 10 kHz.**

**Table 1: A table containing the fitted sites and parameters extracted after SOLA fitting**

| Compound | Experiment | Site / ppm | $C_Q$ / Hz | $\eta_Q$ |
|---|---|---|---|---|
| TiSnSb | C/2 1st discharge | 4.5 | 1740 | 0.617 |
| | | 0.0 | 3311 | 0.687 |
| | 4C 1st discharge | 8.2 | 1736 | 0.223 |
| | | 19.6 | 657 | 0.198 |
| | C/2 1st charge | 12.9 | 0.0 | 0.613 |
| | 4C 1st charge | 1.9 | 3227 | 0.149 |
| | | 9.9 | 557 | 0.102 |
| | C/2 2nd discharge | 6.3 | 2677 | 0.11 |
| | 4C 2nd discharge | -15.0 | 3733 | 0.1 |
| | | 7.3 | 195 | 0.546 |
| Ti+Sn+Sb | C/2 1st discharge | 17.1 | 1064 | 0.68 |
| | | 3.5 | 1497 | 0.414 |
| | C/2 1st charge | 8.17 | 1386 | 0.143 |
| | C/2 2nd discharge | -1.2 | 2199 | 0.692 |
| | | -4.4 | 196 | 0.032 |

The $^{23}$Na MAS NMR spectrum can be fitted using two distinct Na sites, one with a relatively small value of $C_Q$ 1740 Hz and the second with a much larger value of 3311 Hz. This indicates that one of the Na environments is a low symmetry site, whilst the other is a much more symmetrical environment. Allan *e.t al.* observed the formation of amorphous phases of sodiated antimony after the first discharge of TiSnSb against an antimony electrode.[80] They loosely assigned these phases to $\alpha$-$Na_{3-x}Sb$. However, they observed a transition to crystalline $Na_3Sb$ (a more symmetric phase) as discharge progresses which could be what is observed in Figure 12. Looking at published literature regarding *operando* $^{23}$Na sites Stratford *et. al.* suggests a strong contribution from the SEI in the resonance at 10 ppm.[95] Stratford *et. al.* also observed peaks at 50, 75, and −75 ppm which they assign to chains of tin atoms, $NaSn_2$, and $Na_{15}Sn_4$ respectively.[95]

Resonances above 100 ppm were also observed however Stratford *et. al.* determined these to be due to the Knight shift which is indicative of metallic sodium.[95] Using Stratford's work as a basis there may be some contribution at -75 ppm from $Na_{15}Sn_4$ however it is difficult to determine. *Johnston et. al.* observed the formation of $Li_2Sn_2$ and $Li_7Sn_3$ but their experiments were centred around the relaxation of the electrode and therefore are not directly applicable. There is not enough evidence in the literature on the interactions of Na within TiSnSb during sodiation to provide full estimates of the constituents of the NMR spectra however the work of Allan *et. al.* as well as Stratford and Johnston gives an initial starting point for analysis.

To further investigate the behaviour of TiSnSb upon sodiation, a sample of TiSnSb was discharged to 10mV at a rate of 4C. This represents a faster rate for sodium diffusion, where 4 sodium ions are inserted into the structure at a rate of 4 Na atoms per hour. The discharge profile, shown in Figure 13, exhibits a rapid decrease in potential from an OCV of 2.8 to 0.6 V, which can be attributed to the SEI formation. There is then a gradual decrease in potential.

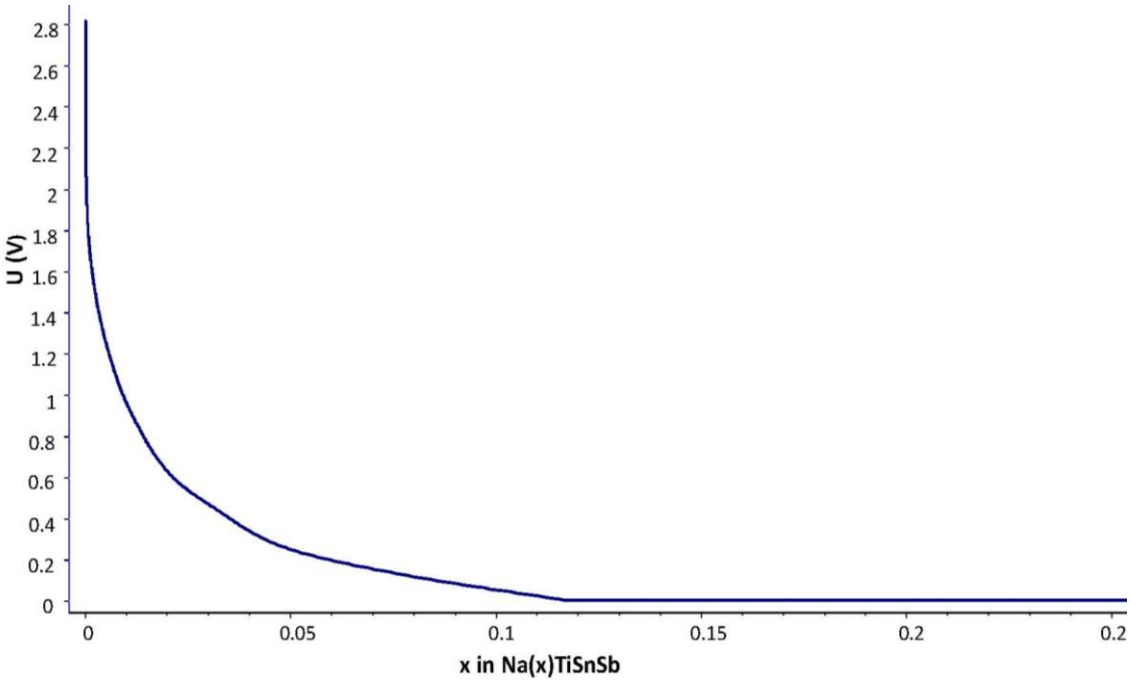


**Figure 13: The potential profile obtained for the sodiation of a sample of TiSnSb at the end of the first discharge. The sample was cycled at a rate of 4C.**

Based on the electrochemical data presented, the sodiation of TiSnSb is believed to proceed via a conversion reaction. In a similar manner to the sample cycled at C/2, no distinct plateaus are observed relating to the sodiation of the electrode.

During electrochemical testing and optimisation, it is important to determine how a material performs at different cycling rates as ultimately in real life applications they will be used at different rates. Since 4C is a faster rate of cycling it results in the faster insertion of Na into the TiSnSb structure. In electrochemistry; faster cycling rates often result in less of the guest species being inserted into the structure. The reduction in inserted Na ions may be due to the very fast rates of diffusion bombarding the structure. Hence, it is not very surprising that only 0.11 Na ions have been inserted into the TiSnSb structure when cycled at 4C.

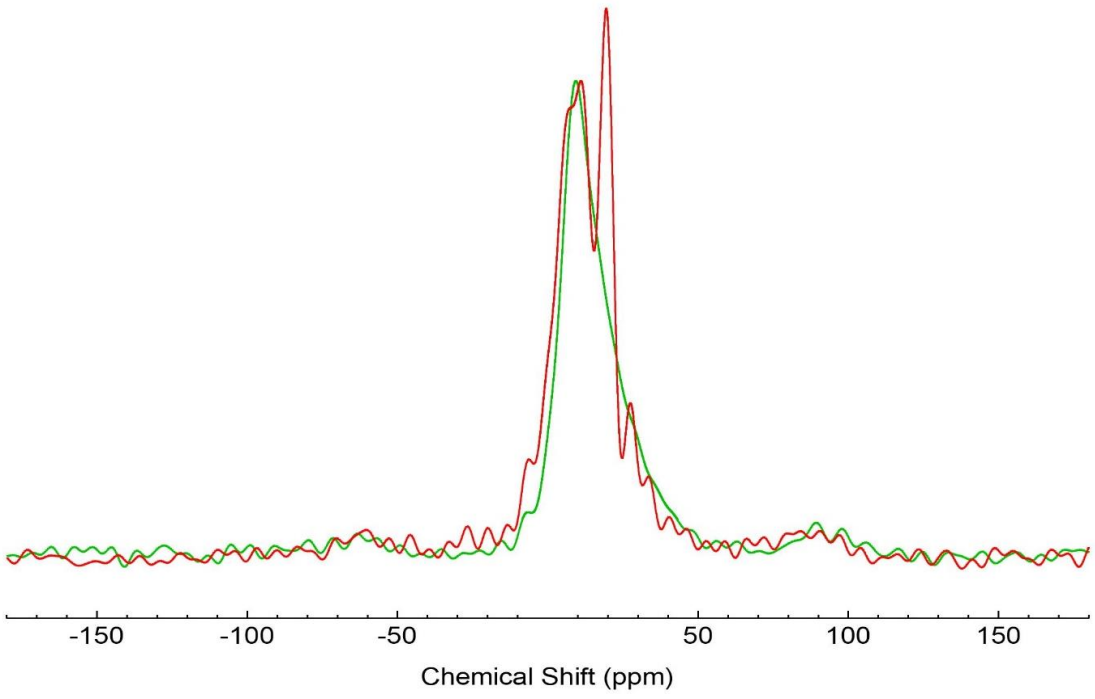


**Figure 14: A composite figure of two $^{23}$Na MAS NMR spectra, obtained for TiSnSb at the end of discharge (sodiation) after cycling at rates of C/2 (green) and 4C (red). The MAS rate was 10 kHz.**

At fast cycling rates it is highly likely that kinetics plays a role in the phases formed. Hence, it is likely that different sodium-containing phases are present at the end of discharge than were observed for C/2, as C/2 rates may be more thermodynamically influenced. The $^{23}$Na MAS NMR spectrum obtained for the sample of TiSnSb cycled at 4C is shown in Figure 14. Also shown for comparison, is the $^{23}$Na MAS NMR spectrum obtained for the sample cycled at C/2. The spectrum obtained for the 4C sample has two resonances; one broad resonance centred at δ = 9.1 ppm, and a sharp resonance at δ = 19.3 ppm. The broad resonance displays some shouldering towards lower chemical shift. Since the resonance at δ = 19.3 ppm is only present in the spectrum corresponding to the sample cycled at 4C, it could be attributed to a kinetic phase resulting from the faster rate of cycling. It could also be one of the highly unstable phases that *Johnson et. al.* discuss in their paper due to the hypothesised kinetic drivers which would then relax if the system was left under OCV conditions.[90] This phase is also not present in the same intensity in further cycles indicating that the phase resolves as cycles progress. As before, it is likely that the large resonance at 9.1 ppm is dominated by SEI contribution.[95]

The results of these experiments tell us that the rate of discharge has an effect on the reaction mechanism of the Na TiSnSb system. Given these differences, further experiments will pit the 4C and C/2 charge rates against each other at other significant points in the cycle profile of TiSnSb.

## 3.2 Behaviour at the end of the first discharge for Ti+Sn+Sb

Previous work in our research group has demonstrated that the nature of the alloy can play a substantial role in the phases formed at the end of the discharge.

More specifically, alloys, *i.e.*, those that have been produced via high energy ball milling (such as TiSnSb described above) can be compared to rough mixtures *i.e.*, those that have not been ball milled but have been manually mixed in a mortar and pestle. Here, the rough mixture refers to a mix of the elemental powders Ti, Sn, and Sb, hereby referred to as Ti+Sn+Sb.

The electrochemical profile for the first discharge of Ti+Sn+Sb against Na is shown in Figure 15. The mixture was cycled at a rate of C/2. When compared to the discharge profile obtained for TiSnSb, Ti+Sn+Sb clearly proceeds through a stepwise reaction, indicating separate reaction steps for the sodiation of Sb and Sn. Starting at an OCV of 2.5 V, there is a drastic decrease in potential to 0.4 V where a plateau forms, believed to correspond to formation of the SEI. Two characteristic plateaus at 0.2 and 0.1 V are then observed before reaching 10 mV.

This profile is characteristic of a material undergoing an alloying reaction.[87] Previous research by Sougrati *et. al*, identified the differing behaviour of mixtures of Ti+Sn+Sb vs. the ternary alloys of TiSnSb with respect to Li, which is in good agreement with the data collected here, indicating that both lithium and sodium

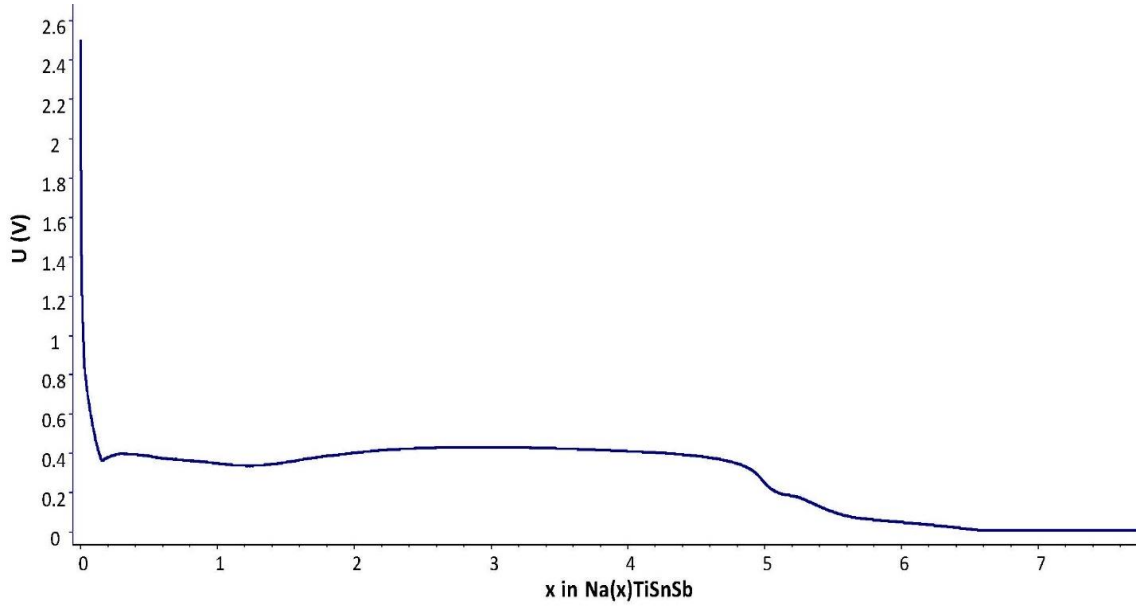


**Figure 15: The potential profile obtained for the sodiation of a sample of Ti+Sn+Sb to the end of the first discharge. The sample was cycled at a rate of C/2.**

react similarly with Ti+Sn+Sb mixtures. According to work by Marino *et. al*, on the lithiation of rough mixtures of Ti+Sn+Sb, the first plateau in the discharge profile can be assigned to the lithiation of antimony to form $Li_3Sb$, and the following steps can be assigned to the lithiation of metallic tin.[86]

Given the similarities of the system and the species being inserted into the structure, this may be useful in determining the phases formed during sodiation. However, it is important to remember that the size differences between Li and Na ion radii affects the phases produced heavily. Hence, the differences in reaction mechanism for Ti+Sn+Sb vs. TiSnSb could be attributed to larger domains associated with the individual elements in the electrode. This would result in sequential sodiation as each reaction with a different element will enable the discharge process to progress further. Hence, each step corresponds to a different voltage plateau.

Unlike the discharge profile for TiSnSb, 6 Na atoms per formula unit can be inserted into Ti+Sn+Sb. This is considerably more than that for the ternary alloy TiSnSb. This can be attributed to the impact of the ball milling on the internal structure of the electrode. An electrode which is less refined will have larger internal phases of each species. This means that the particle grain sizes are larger hence there will be greater internal spacing, which will enable a greater degree of sodium diffusion into the structure. The number of Na atoms inserted is consistent with that observed for the lithiation of Ti+Sn+Sb, albeit at a much lower rate of C/10. This is interesting as it could be indicating that the structure of the mixture is not as affected by the size of the electroactive ion when compared to that of the ternary alloy.[87]

Figure 16 displays the $^{23}Na$ MAS NMR spectrum obtained for Ti+Sn+Sb at the end of the first discharge. The spectrum exhibits a single relatively broad resonance centred at $\delta = 6.7$ ppm. And a small feature is also observed at $\delta = 19.5$

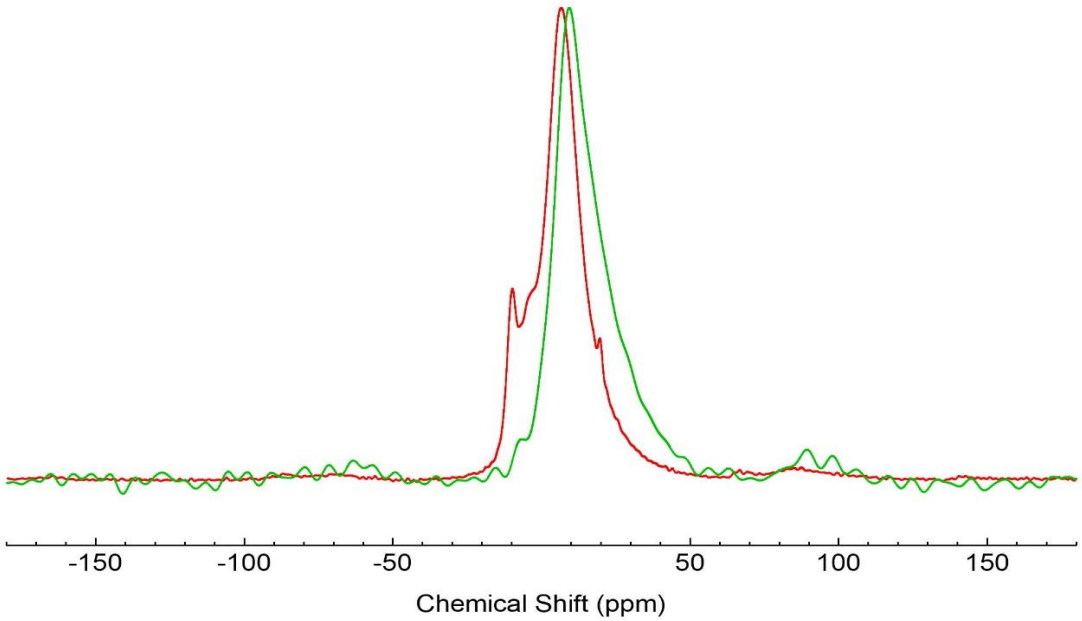


**Figure 16: An overlay of the $^{23}$Na MAS NMR spectra obtained for Ti+Sn+Sb (red) and TiSnSb (green) at the end of the first discharge (sodiation). Both samples were cycled at C/2 and the MAS rate used was 10 kHz.**

ppm. This is similar to that observed for the 4C TiSnSb, so may well be one of the unstable kinetic phases which can be formed through both conversion and insertion reaction mechanisms. The fit of the spectrum shows one high symmetry, 557 Hz, environment and one with very low symmetry 3227 Hz. Given that the 9.9 ppm environment is probably attributed to the SEI, the remaining broad 1.9 ppm environment may be an alternative environment produced from via the insertion reaction.

The presence of this feature could also be indicative of multiple overlapped resonances. In Figure 16, the spectrum obtained for Ti+Sn+Sb has been overlaid with that obtained for TiSnSb at the end of the first discharge. In such cases it is difficult to determine from a one-dimensional spectrum precisely how many sites are present and, often, two-dimensional techniques are needed such as multiple-quantum MAS (MQMAS) are needed. However, in this case it was

not possible to acquire a $^{23}$Na MQMAS spectrum in a suitable timeframe owing to extremely small sample quantities. In order to acquire such as spectrum it would take several days, and multiple electrodes would need to be combined. It is also important to note here that when multiple electrodes are combined the electrochemical performance must be identical, otherwise they are not comparable. Often, obtaining electrodes with identical performance this is challenging to achieve. As a result, this was outside the scope of the current study.

## 3.3 Behaviour at the end of the first charge for TiSnSb

Electrochemical studies of the first discharge can provide insight into the reaction mechanism during the initial sodiation of the structure. The next logical step in analysis is to examine the behaviour of the system when the sodium has been removed, *i.e.,* at the end of the charge (de-sodiation) process. The electrochemical profile for the first charge of TiSnSb at a rate of C/2 is shown in Figure 17. During discharge (sodiation) the same rapid decrease in potential to 0.6 V is observed, which is attributed to SEI formation. After reaching the end of discharge, a reverse current is applied, and the system is charged (de-sodiated) to 2.5 V. During this charge process; Na ions are removed from the TiSnSb structure, ideally producing the reverse discharge reaction mechanism; if the two processes are fully identical then it indicates that the system is reversible. It is important to note that after charging the system does not fully return to equilibrium. This is a result of the formation of the SEI, *i.e.*, the irreversible trapping of some of the Na in the SEI layer. This creates an irreversible capacity loss during the first full cycle, meaning that not all the Na ions inserted during the first cycle are fully removed. This behaviour is in good agreement with other

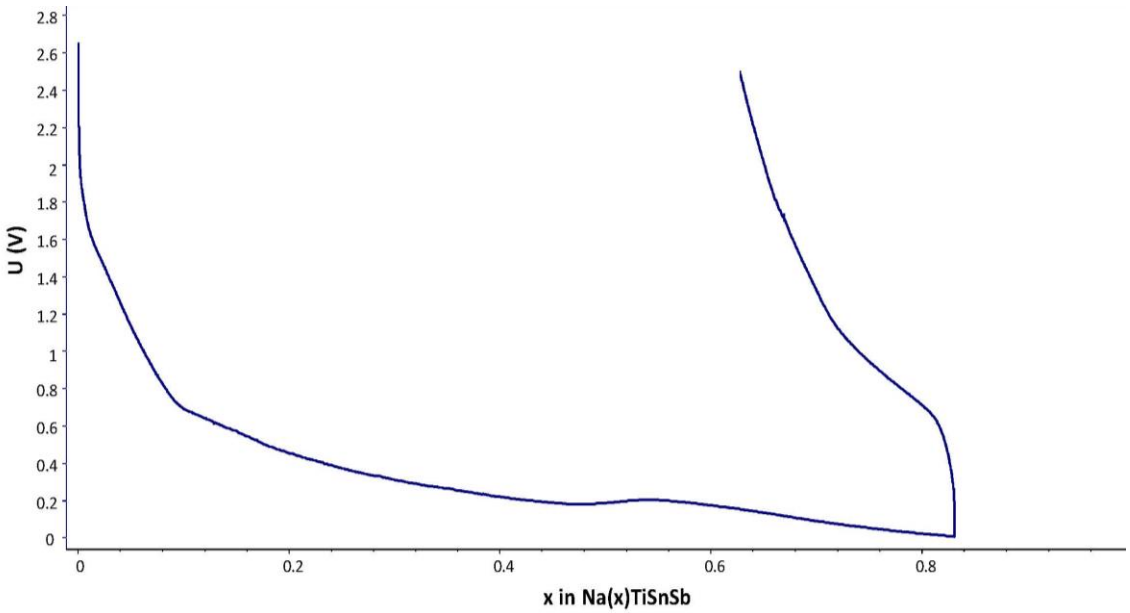


**Figure 17: The discharge/charge profile obtained for a sample of TiSnSb at the end of the first charge (sodiation). The sample was cycled at a rate of C/2.**

similar materials and systems being proposed as possible negative electrode materials.

Interestingly, the charge profile appears to demonstrate a different reaction mechanism relative to that observed during discharge. The charge cycle appears to undergo two different processes during de-sodiation; a rapid increase in potential from 0 to 0.6 V and a much slower, gradual change in potential from 0.6 to 2.5 V, as demonstrated in Figure 17. The first phase of the charge mechanism is the rapid increase in potential related to the overpotential of removing Na from the system. After this, sodium appears to be removed from the structure and is likely to be indicative of the simultaneous removal of Na from the various $Na_xSn_{1-x}$ and $Na_xSb_{1-x}$ phases formed.

The $^{23}Na$ MAS NMR spectrum obtained for the sample of TiSnSb at the end of the first charge is shown in Figure 18. The spectrum obtained exhibits poor signal-to-noise which is to be expected as there is very little Na in the system relative to that obtained for the discharged sample. A single resonance is observed, centred at $\delta$ = 11.9 ppm. This is the expected outcome as the species

formed upon charge should be different from those at the end of discharge. This leads to the conclusion that no irreversible species have been produced in large amounts. This resonance has also not been observed in previous spectra, at least not a great intensity. Fitting the data produced a fit with only one dominant resonance at 12.9 ppm, see Table 1. This fit produced an environment with a $C_Q$ of 0 indicating a very high symmetry environment. Whilst this single environment could be indicative of the original starting material, Allan *et. al.* found that after charge, their antimony electrode reverted to a mixture of amorphous and crystalline antimony, not just a crystalline system.[80] The experiment here may provide evidence that TiSnSb has better structural retention than has previously been observed.

By overlaying the spectra obtained at the end of the first discharge and the end of the first charge, it is possible to determine the remaining Na environments *i.e.,* those that are trapped in the SEI therefore and contribute to the overall loss in capacity. This information can be used to estimate the contribution of the SEI.

In Figure 18 this has been accomplished by normalising both spectra and subtracting the differences between the two to create a third line (blue). Hence, this residual spectrum can be used to fit subsequent data sets and determine the

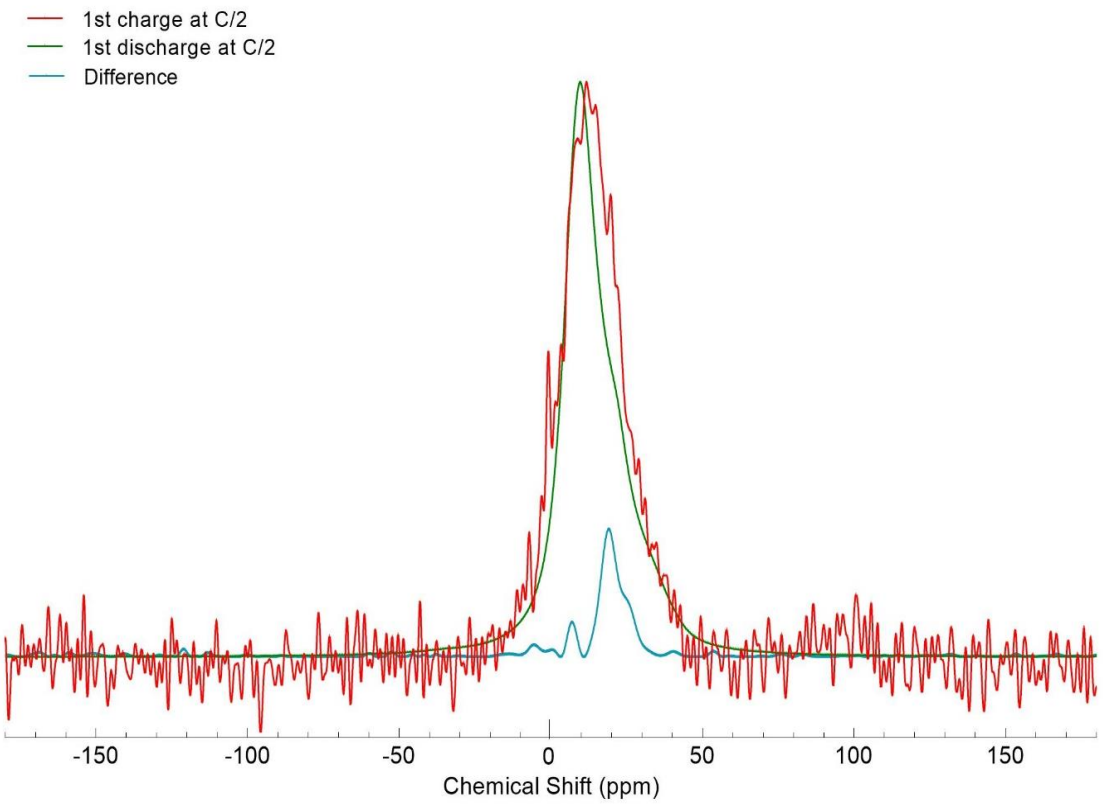


**Figure 18: An overlay of the $^{23}$Na MAS NMR spectra obtained for TiSnSb, cycled at a rate of C/2 to the end of discharge (green) and the end of charge (red). The MAS rate was 10 kHz. Also shown in blue for comparison is the difference between the two.**

contributions from Na trapped in the SEI relative to those of the Na-Sn and Na-Sb phases formed. This experiment indicates that the SEI contribution is centred around 20 ppm but is small in comparison to the intensities of the signal from discharge and charge phases.

The electrochemical profile obtained for the first charge of TiSnSb at 4C is shown in Figure 19. Identical behaviour to that observed for the discharge of TiSnSb is observed here, indicating reproducibility however full discharge is achieved with fewer sodium-ions. This may be due to small variations in electrode size or it could be indicative of other variation in the reaction system.

The charge potential profile obtained during charge is very similar to that obtained at C/2 with similar mechanisms indicated; *i.e.,* one involving very little sodium and a second more extensive de-sodiation step. The similarities between

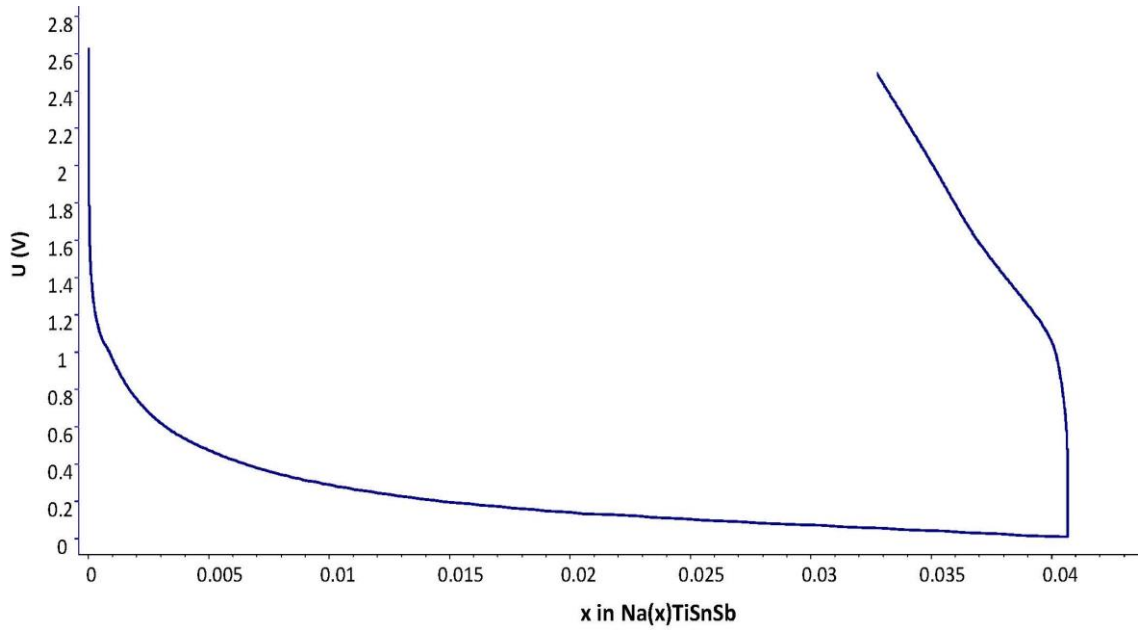


**Figure 19: The potential profile obtained for a sample of TiSnSb at the end of the first charge (de-sodiation). The sample was cycled at a rate of 4C.**

the two profile shapes indicate that similar mechanisms may be occurring upon de-sodiation, albeit with fewer sodium ions involved due to the faster rate of sodium insertion and removal.

In a similar manner to the sample cycled at C/2, a large irreversible capacity is observed, indicating Na ions irreversibly trapped in the SEI. Again, this is in good agreement with other, similar systems tested as negative electrode materials.

The $^{23}$Na MAS NMR spectrum obtained for the sample of TiSnSb at the end of charge at a rate of 4C, can be seen in Figure 19. A single, relatively broad asymmetric resonance is observed at $\delta$ = 9.7 ppm. The fitted parameters reveal two sites one at 9.9 ppm and one at 9.1 ppm. Both sites are low symmetry environments. Figure 20 also includes the charge and discharge spectra for 4C. The differences in the features observed could be indicating where Na is in the

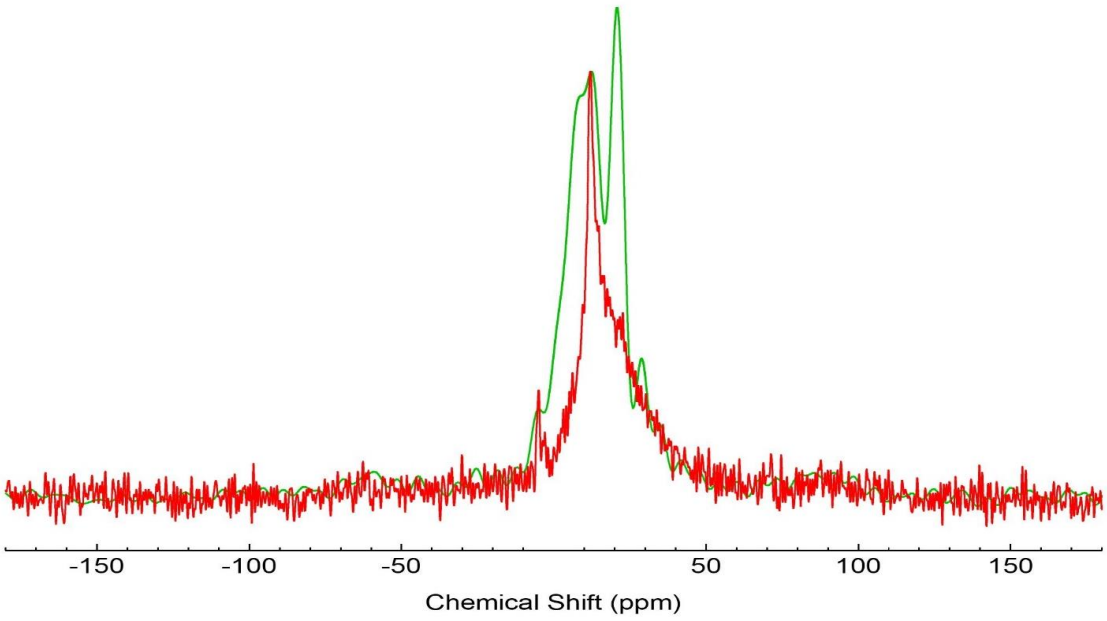


**Figure 20: A composite figure of two $^{23}$Na MAS NMR spectra for TiSnSb at the end of the first discharge (green) and the first charge (red). They were cycled at a rate of 4C. The MAS rate was 10 kHz.**

structure and potential mechanisms for the sodiation and de-sodiation of samples, especially in the case of the strong sharp resonance at $\delta = 9.7$ ppm.

## 3.4 Behaviour at the end of the first charge for Ti+Sn+Sb

The first charge profile for Ti+Sn+Sb is shown in Figure 21. The profile exhibits obvious sequential steps during de-sodiation suggesting that the mechanism for charge is also via an alloying reaction, similar to that of the discharge process. The discharge profile associated with this experiment is consistent with that of previous experiments thereby demonstrating reproducibility. Again, owing to the formation of the SEI there is a large irreversible capacity. At the end of the first charge the number of sodium ions remaining in the electrode is 4.4. When compared to the TiSnSb electrode, this is a much greater loss of sodium. This is likely a consequence of the larger grain spacing in the unrefined Ti+Sn+Sb, which

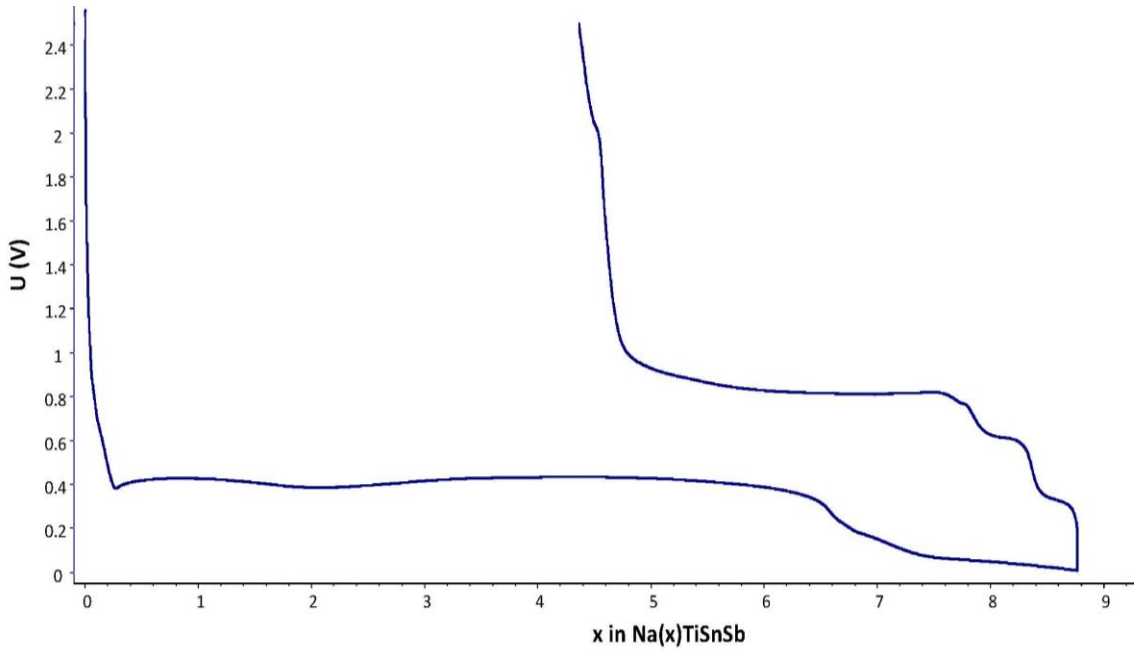


**Figure 21: The potential profile for Ti+Sn+Sb at the end of the first de-sodiation (charge). The sample was cycled at a rate of C/2.**

enables the sodium to diffuse out of the structure at a faster rate and hence, for more sodium ions to be removed during charge.

The $^{23}$Na MAS NMR spectrum obtained for the sample of Ti+Sn+Sb cycled to the end of the first charge at rate of C/2 exhibits a single resonance at $\delta$ = 10.8 ppm, see Figure 22. When fitted one environment at 8.17 was elucidated which is not something that has been previously observed.

When compared to the $^{23}$Na MAS NMR spectrum obtained at the end of the first discharge for Ti+Sn+Sb there is considerable overlap between the two, as shown in Figure 23. However, the shift has migrated which suggests that different environments are present. This suggests that the Na environments remaining at the end of the first charge are similar to those at the end of the first

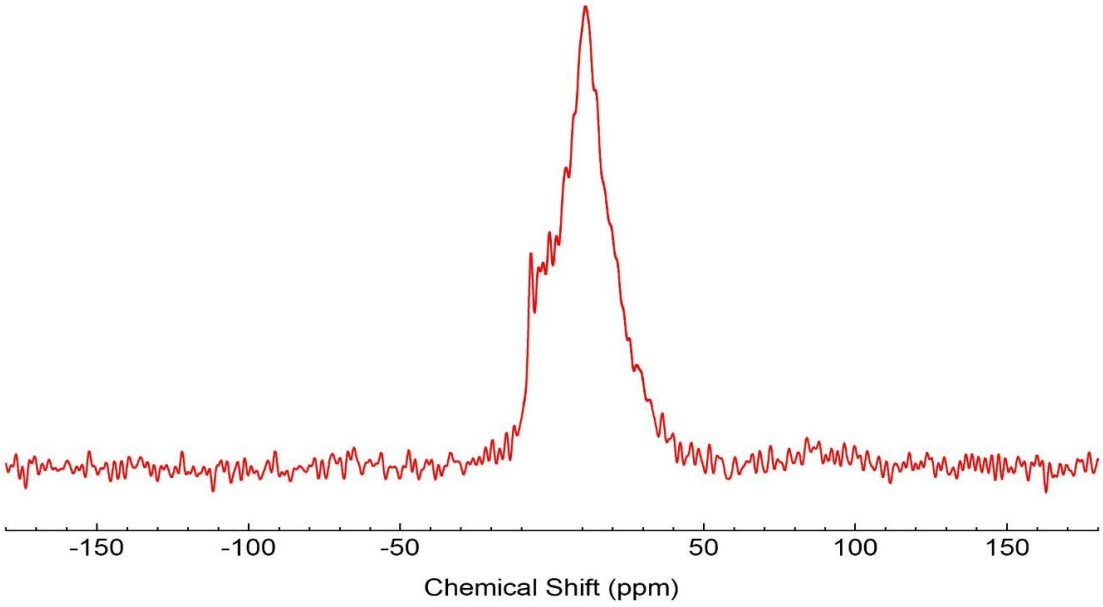


**Figure 22: $^{23}$Na MAS NMR spectrum obtained after electrochemical cycling of Ti+Sn+Sb until charge, cycled at a rate of C/2. The MAS rate was 10 kHz.**

discharge. Hence, it is challenging to accurately decipher the Na environments corresponding to those trapped in the SEI.

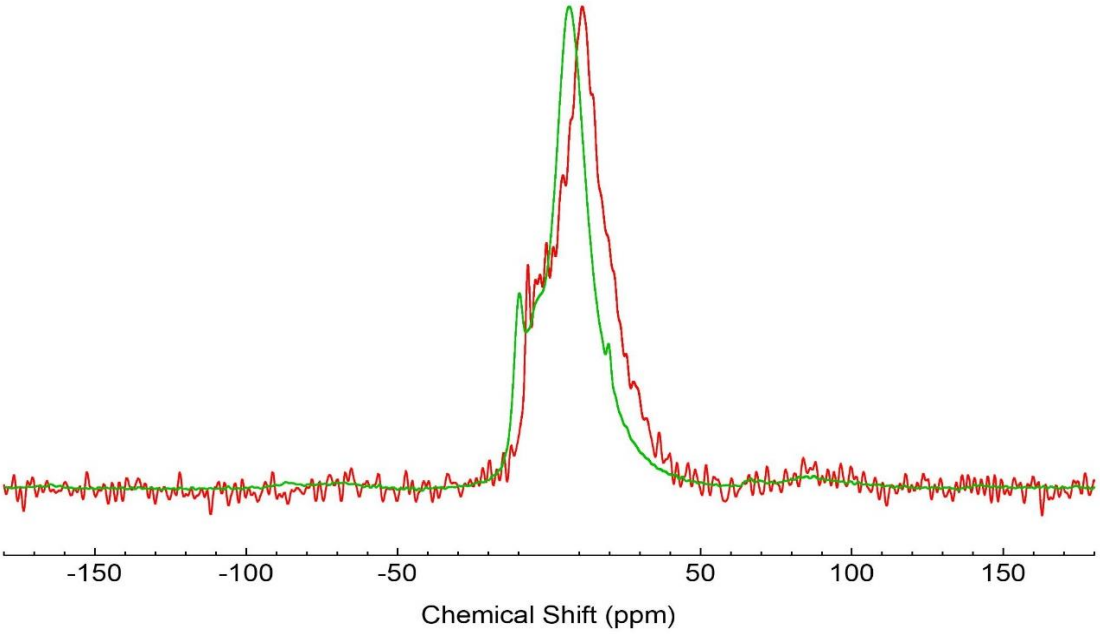


**Figure 23: A composite figure of the charge (red) and discharge (green) $^{23}$Na MAS NMR spectra for Ti+Sn+Sb cycled at a rate of C/2. The MAS rate was 10 kHz.**

## 3.5 Behaviour at the end of the second discharge for TiSnSb

By monitoring the second discharge profile, we can observe the behaviour of the electrode after formation of the SEI. The discharge profile associated with the second discharge of TiSnSb cycled at C/2 is shown in Figure 24. The electrochemical profile obtained is in good agreement with that of the first discharge; they both possess similar shapes and the number of Na ions is also identical indicating that the system is reproducible.

From Figure 24 it can be extrapolated that approximately 0.6 sodium ions are irreversibly lost after the first discharge. It is likely that these are associated with the formation of the SEI and other side products formed. As a result, during the second discharge fewer Na ions are inserted into the structure and a loss of capacity is observed. This is indicated on Figure 24 by an arrow. To determine whether this behaviour is consistent with increasing cycle number, multiple cycles would need to be completed. At present, this is outside of the current scope of the project as it would require experiments extending across multiple days in order to gather the required data.

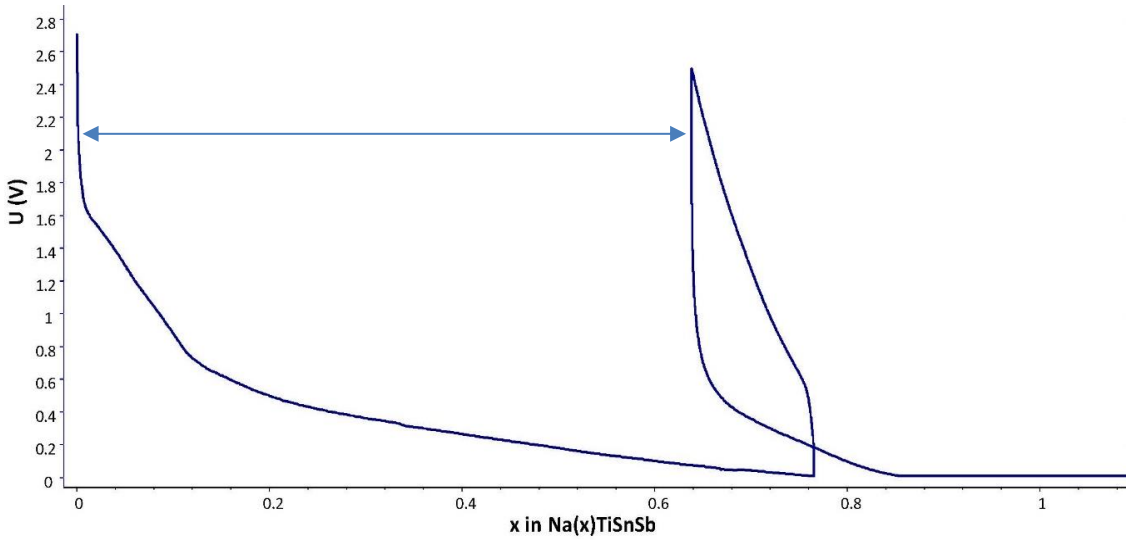


**Figure 24: The potential profile for a sample of TiSnSb at the end of the second discharge (sodiation). The sample was cycled at a rate of C/2**

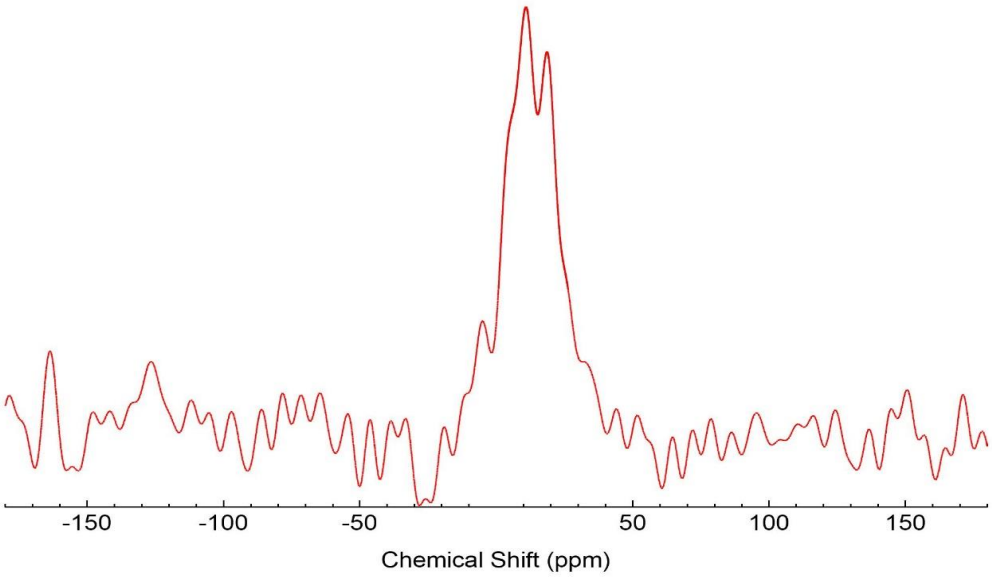


**Figure 25: $^{23}$Na MAS NMR spectrum obtained after electrochemical cycling of TiSnSb to the second discharge, cycled at a rate of C/2 The MAS rate was 10 kHz.**

The $^{23}$Na MAS NMR spectrum obtained for the second discharge of TiSnSb at C/2 is shown in Figure 25. This spectrum has a single broad resonance centred at $\delta$ = 10.5 ppm. There appears to be evidence of a small shoulder at $\delta$ = 12.6 ppm indicating some peak asymmetry This signal demonstrates a poor signal-to-noise ratio which affects the degree to which it can compared to other data.

When compared to the $^{23}$Na MAS NMR spectrum obtained at the end of the first discharge, the position of the resonance has shifted by 4 ppm, which suggests a change in the sodium-containing species obtained at the end of each discharge. This is unusual because at the end of each cycle it is expected that the same phases will form, with the same Na environments. It is possible that further sodiation has occurred during the second cycle and species with a higher sodium stoichiometry have been produced.

The electrochemical profile for the second discharge of TiSnSb at 4C is shown in Figure 26. In a similar manner to the electrochemical data obtained for TiSnSb at the end of the first discharge, fewer Na ions have been inserted into the structure. This is ultimately due to the faster rate of cycling. Hence, both the first

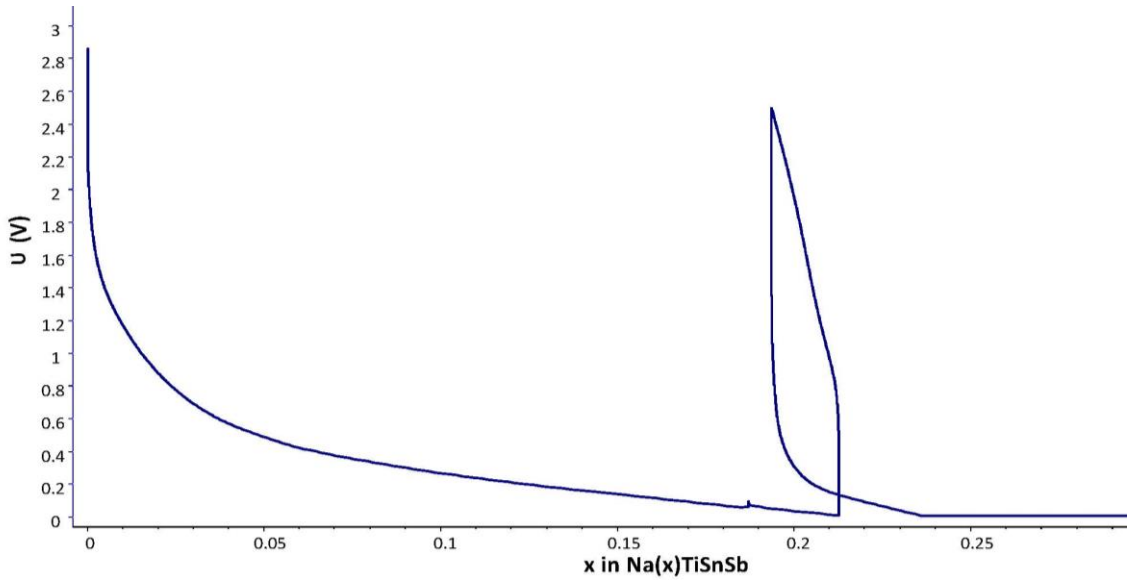


**Figure 26: The potential profile for a sample of TiSnSb at the end of the second discharge (sodiation). The sample was cycled at a rate of 4C.**

and second discharge profiles indicate that faster cycling rates result in fewer Na ions being inserted into the structure when compared to the samples cycled at C/2. If multi-cycle experiments were undertaken over time, we would expect to see this contribute to an overall loss in capacity.

The $^{23}$Na MAS NMR spectrum obtained for a sample of TiSnSb at the end of the second discharge cycled at 4C, shown in Figure 27, exhibits a broad resonance centred at $\delta$ = 5.1 ppm which a sharp side feature at $\delta$ = 19.5 ppm, and at -7.6 ppm. This very sharp feature (19.9 ppm) was also observed in the 1$^{st}$ discharge spectrum which indicates that there is a phase which is repeatable formed upon discharge for the 4C rate. Fitting this proved difficult and could be interpreted through two directions. Either one dominant resonance with 2 sharp side features or a resonance which has a very large $C_Q$ values either side of a central resonance. This second fit is included in Table 1.

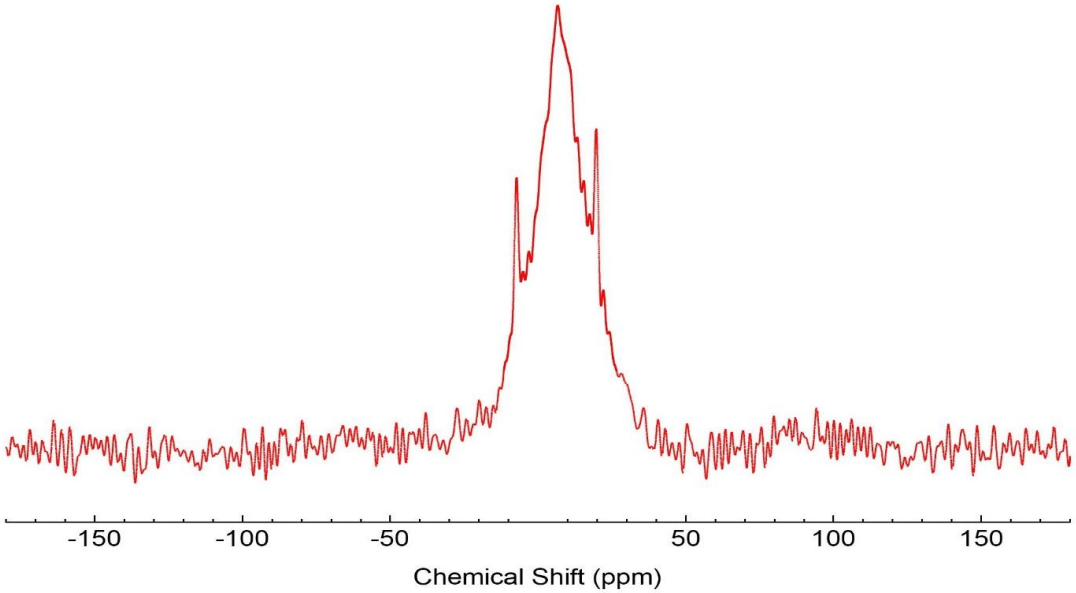


**Figure 27: $^{23}$Na MAS NMR spectrum obtained after electrochemical cycling of TiSnSb to the second discharge, cycled at a rate of 4C. The MAS rate was 10 kHz.**

When compared to the $^{23}$Na MAS NMR spectrum obtained at the end of the first discharge of TiSnSb at 4C, Figure 28, there is a clear obvious reduction in the intensity of the peak δ = 19.5 ppm. This could be indicative of a transient kinetic phase which is formed and removed during the first cycle but does not form during the second cycle. It may be the case that the destruction caused to the electrode due to the higher rate of sodium insertion causes irreversible changes. These changes then go onto affect the reaction mechanism of later cycles.

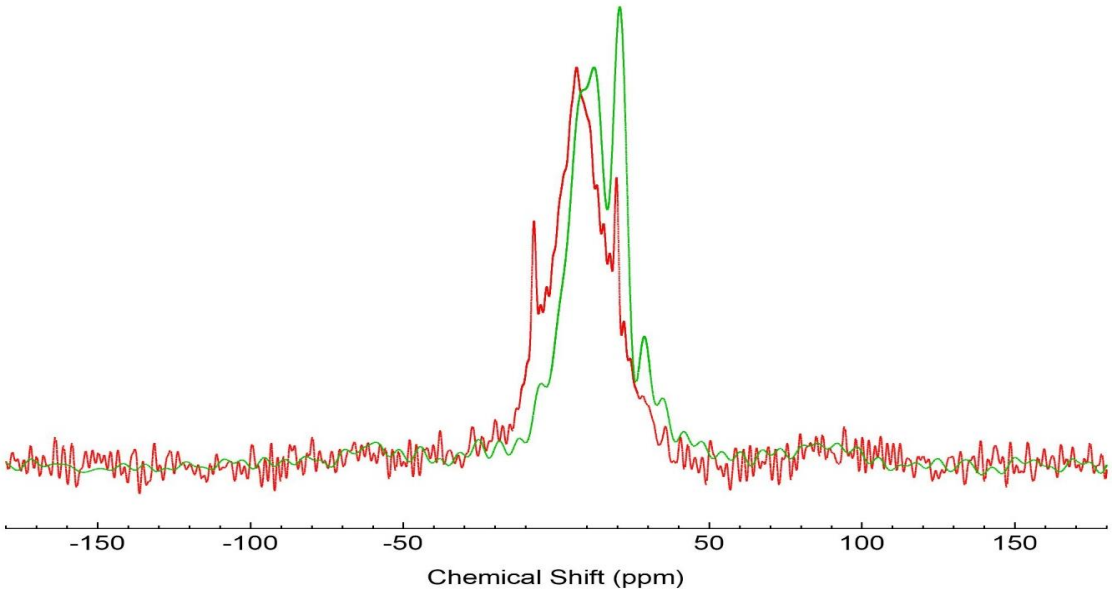


**Figure 28: A composite figure of the first (green) and second (red) discharge $^{23}$Na MAS NMR spectra for TiSnSb, cycled at a rate of 4C. The MAS rate was 10 kHz.**

## 3.6 Behaviour at the end of the second discharge for Ti+Sn+Sb

The electrochemical profile for the second discharge of Ti+Sn+Sb, Figure 29, shows good agreement with the data previously collected at the end of the first discharge and charge in terms of plateau characterisation. However, there are some discrepancies observed regarding the total number of sodium ions inserted. From the precise form of the profile it can be noted that the features and shape of the second discharge profile are less well defined than for the first. This may be indicative of different reaction pathways occurring for this material.

At of the end of the first charge, 4 sodium ions per formula unit remain in the Ti+Sn+Sb structure and at end of the second discharge 6 sodium ions have been inserted into the structure. This is slightly more than was inserted during the first discharge. The increase could be due to a greater diffusion of the Na ions further into the structure than was previously possible.

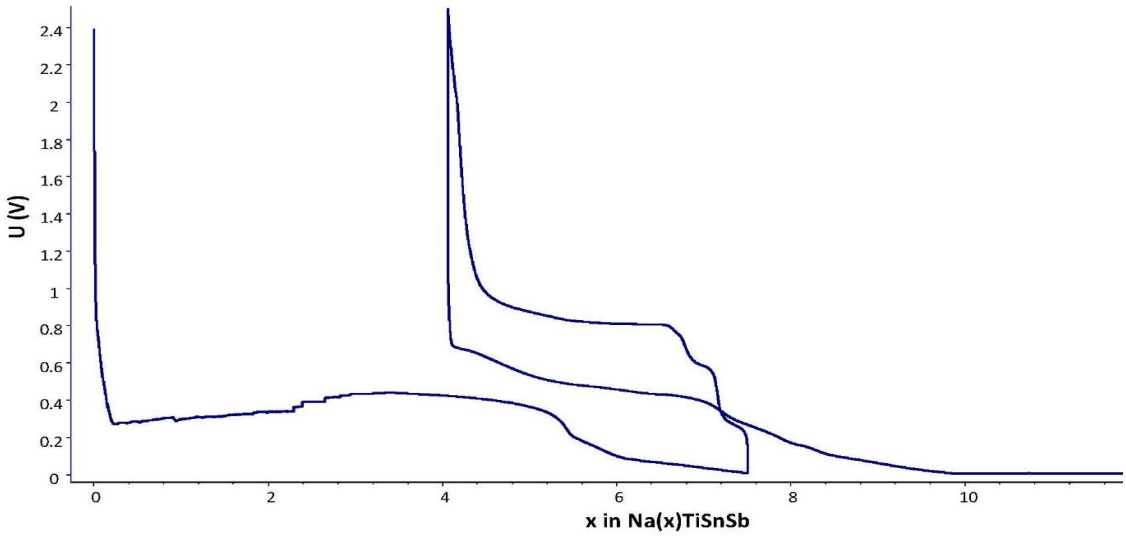


**Figure 29: The potential profile for a sample of Ti+Sn+Sb at the end of the second discharge (sodiation). The sample was cycled at a rate of C/2.**

The $^{23}$Na MAS NMR spectrum for Ti+Sn+Sb cycled at C/2 to the end of the second discharge is shown in Figure 30. The spectrum contains a single resonance at 6.4 ppm with a small feature at $\delta = -4.6$ ppm. This small additional feature could be indicative of a different sodium environment which has evolved or could be a small indicator of a quadrupolar species as seen in the second discharge $^{23}$Na MAS NMR spectrum for TiSnSb (Figure 27).

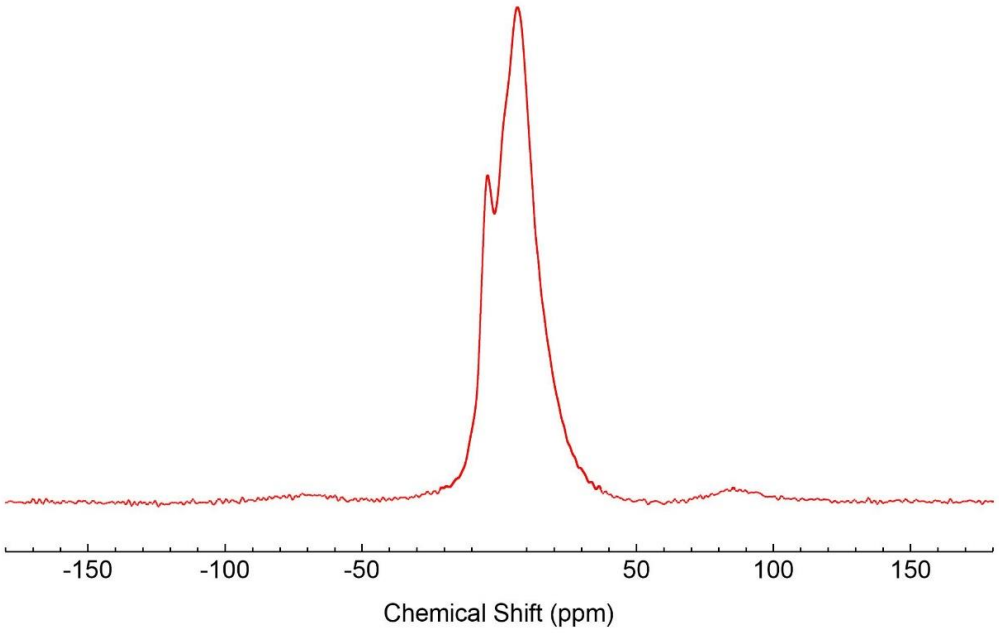


**Figure 30: $^{23}$Na MAS NMR spectrum obtained after electrochemical cycling of Ti+Sn+Sb to the second discharge, cycled at a rate of C/2. The MAS rate was 10 kHz.**

When compared, to the $^{23}$Na MAS NMR spectrum, Figure 31, obtained at the end of the first discharge, there is sufficient overlap and similarities between the two, indicating that the environments produced at the end of the second and first discharge are closely related. The main difference between the two is a slight increase in intensity of the feature at δ = — 4.5 ppm in the spectrum corresponding to the second discharge. This may be indicative of a change in reaction mechanism where a species is formed in greater quantity after repeated discharges. Given that this is unlikely to be a cumulative increase in an irreversible species it may therefore be due to a thermodynamically stable phases which is less affected by the quantities of sodium but instead by its own stability within the system.

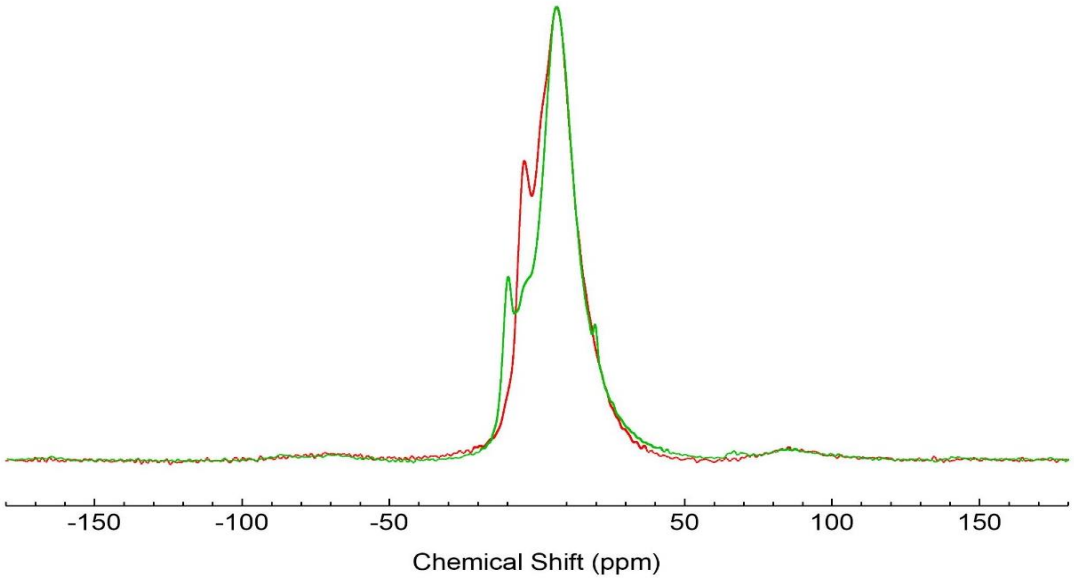


**Figure 31: A composite figure of the 1st discharge (red) and 2nd discharge (green) profiles for $^{23}$Na MAS NMR spectra for Ti+Sn+Sb, cycled at a rate of C/2. The MAS rate was 10 kHz.**

# Chapter 4 Conclusions

This study has demonstrated that TiSnSb has the potential to be viable as negative electrode for sodium-ion batteries. The electrode operates via a conversion mechanism which is comparable to the behaviour exhibited by other ternary alloy electrode materials. Electrochemical profiles were reliably produced with potentials of 2.6 – 2.8 V. Evidence of voltage hysteresis is present however exploration of the behaviour of TiSnSb across multiple cycles was beyond the scope of this current study (see Chapter 5). Some information has been gained about the reaction mechanisms occurring within the system. It is possible to tentatively assign the reaction mechanism to;

$$\mathrm{TiSnSb} + n\mathrm{Na} \leftrightarrow y\mathrm{Na}_{1-x}\mathrm{Sn} + y\mathrm{Na}_{1-x}\mathrm{Sb} + \mathrm{Ti} \qquad (4.1)$$

Based on the evidence provided for the lithium system by Johnston *et. al.* and it's similarities to the Na system.

The conversion mechanism evident from in this research is directly related to the ball milled fine structure of the alloy material as rougher mixtures (Ti+Sn+Sb) operate via alloying reactions leading to different electrochemical performances which are characterised by distinct plateaus in the voltage profile.

TiSnSb as a material is quite sensitive to the rate of sodium insertion, evidenced by the changes between the 4C and C/2 potential profiles. This indicates that the structure is not particularly stable and is further demonstrated by the differences between the $^{23}$Na MAS ssNMR spectra for each step of the electrochemistry. This is likely due to the overpotential of the electrode species where less Na ions are able to be added regardless of the starting voltage.

Overall, the TiSnSb system has a better operating voltage compared to other Na anode systems such as metal oxides (2.6 compared to 0.3 V). However, the lack of insight into the performance of TiSnSb across multiple cycles and the capacity it could maintain across that time does not allow for much comparison to alloying anode materials such as pure metallic Sn, Sb, As, and Ge. These alloying materials often experience quite drastic volume expansion upon cycling (see 1.3.3). It is not known whether TiSnSb also experiences a volume expansion across cycles but further XRD experiments could be conducted to determine this.

Overall this research adds to the body of literature surrounding TiSnSb by adding $^{23}$Na ssNMR data. The research agrees with previous published work on $^{23}$Na ssNMR and tin by Stratford *et. al.* which highlighted the contribution of the SEI within the spectra, however this study highlights that the contribution is not absolute and that further research is needed by *ex situ* MQMAS and XRD to elaborate on the phases formed.[95] There is still a lot of work needed to evaluate whether TiSnSb (or another related compound) has the potential to make the Na ion battery a viable option for industrial or commercial ESS applications.

# Chapter 5 Further Work

The results of this study have been important for expanding the knowledge of the interactions of TiSnSb with a Na system. However, further work can still be done to investigate the reaction and internal mechanisms of the system.

The first step would be to conduct studies of the system across longer range cycling i.e. 20 or 50 cycles. During this research project it was not possible to conduct longer experiments of extensive cycle length due to limitations on equipment and the nature of the preparatory process for $^{23}$Na MAS NMR experiments where the electrode had to be processed and analysed as quickly as possible once off the electrocycler. Experiments conducted across multiple cycles would provide insights into the longevity of the system and would be important for evaluating whether the system has commercial applications or uses. Industrial and commercial systems require systems which can operate at sustained capacities for over 500 cycles, hence, if TiSnSb could operate with little capacity loss over long periods it would be an important addition to battery research. Even a sustained capacity across 100 cycles would be beneficial for further development of ternary conversion electrodes for N ion batteries.

Further investigations could also be conducted into the behaviour of the system at lower C rates. In this study the C/2 rate was more informative and providing more information about the system than the 4C rate. It is hoped that using even slower charge/discharge rates would provide even more information, possibly revealing more of the reaction mechanism by revealing further plateaus or changes in potential in the system.

An additional experiment could also study the relaxation of the system under OCV conditions to examine the evolution of the phases formed. Johnston *et. al.* found that that TiSnSb under Li conditions produced a series of unstable phases throughout discharge and it is possible that the Na system also produces equivalent phases. Observing the evolution of these species could be useful for the Na

Many of the comparative and similar studies mentioned in this thesis used different analytic techniques to examine their respective systems. X-Ray Diffraction, $^{119}$Sn Mössbauer, and *in situ*, studies would all be good avenues to pursue in order to investigate the situation further and help to provide good direct comparisons to other literature studies. However, the technical requirements of these experiments are particular and they are not a direct priority compared to cycle length and cycle rate experiments.

# Chapter 6 Appendix

## 6.1 Seminar Summaries

**Single-molecule studies with nanopores and nanopipettes**

Tim Albrecht is a professor at the University of Birmingham and is the universities current chair of physical chemistry. The research in his group focuses on the charged interfaces and charge transfer within nanoscale environments. His talk focused on the novel development of nanopore sensing regarding DNA fingerprinting and profiling.

The Albrecht group have developed a unique sensory technique using an insulating membrane within an electrolyte/DNA solution such that a translocation event can prompt a decrease in potential. The timespan of this drop is indicative of the length of DNA passing through the potential gate and hence differentiation between molecules is possible. It is also possible to distinguish structural features of the DNA based on the shape of the translocation event produced.

This unique sensory technique has direct consequences for the fields of DNA sequencing and DNA profiling. Functionalising the biological pore with specific molecules can allow for amino acid specific reactions to provide knowledge of the DNA sequence. Also, a combination of two different functionalised sites using γ-PNA (peptide nucleic acids) could allow for fingerprinting to occur due to allow for distinguishing translocation events to

occur. Future research on this topic in the Albrecht group is focused on using channel-splitting to improve low-current detection.

**In situ EXAFS studies of electrocatalysts for fuel cells and water electrolysers**

Professor Andrea Russell is a professor of physical electrochemistry at the University of Southampton, she is also the director of programmes for chemistry at Southampton. Her research focus is on the application of spectroscopic methods to the study of electrode/electrolyte interfaces with an emphasis on electrocatalysts and electrode materials for a variety of batteries and sensors.

Within an alcohol fuel cell, *N*-butanol decomposes into carbon dioxide and electrons as part of direct alcohol fuel cells. These fuel cells require catalysts to oxidise CO in order to maintain cell efficiency. In practise catalysts can be modified such as Pt modified with Sn to assist with C-C bond breaking. The Russell group use *in situ* EXAFS (Extended X-ray Absorption Fine Structure) to provide information on the mass of neighbours, distances, and radial distributions from the elasticity of the back scattering within bimetallic catalysts, such as Ru:Pt. Their aim is to understand how the structure of the catalysts influences its activity and stability.

They found it is possible to use Controlled Surface Reactions (CSR) of ruthenium atop carbon to allow for manipulation of ruthenium placement within the surface layers using oxidation. This leads to a dynamic catalytic surface which is influenced by environmental conditions. Interestingly Professor Russel's group found CO adsorption due to changes in data produced from two neighbours. It is possible to bond multiple CO with specific surface placement as this is not a uniform flat surface due to the presence of surface defects and edges which provide high energy sites for reactions.

## Seminars Attended

**Investigations of halide perovskites for optoelectronic applications: Tuning properties and searching for environmentally benign alternatives.**

*Professor Patrick Woodward, Ohio State University*

11 October 2017

**Casting iron in softer catalytic roles**

*Professor Robin Bedford, University of Bristol*

25 October 2017

**Disorder in inorganic solids: Exploiting Multinuclear NMR spectroscopy and DFT calculations**

*Professor Sharon Ashbrook FRSE, University of St Andrews*

1 November 2017

**Cell penetration and Membrane fusion: Two sides of the same coin**

*Professor Pavel Jungwirth, Institute of Organic Chemistry and Biochemistry, Czech academy of sciences.*

15 November 2017

**Single-molecule studies with nanopores and nanopipettes**

*Professor Tim Albrecht, University of Birmingham*

29 November 2017

**RSC Corday-molecule studies with nanopores and nanopipettes: Probing protein aggregation in small volumes**

*Professor Tuomas Knowles, University of Cambridge*

6 December 2017

**RSC Bourke Award lecture – Density functional theory: It's impact in Chemistry and beyond.**

*Professor Kieran Burke, University of California, Irvine*

15 January 2018

**In situ EXAFS studies of electrocatalysts for fuel cells and water electrolysers**

*Professor Andrea Russell, University of Southampton*

17 January 2018

**Better UV filters for better life**

*Dr Vasilios Stavros, University of Warwick*

24 January 2018

**Molecular Processes in intercalation and redox flow batteries**

*Professor Ulrich Stimming, Newcastle University*

21 February 2018

**f-elements as a playground for magnetic resonance**

*Dr Nicholas Chilton, Manchester University*

9 April 2018

**Staring down the barrel: what has Europium revealed in 15 years**

*Dr Robert Pal, Durham University*

9 April 2018

**Centenary Prize Lecture: The importance of questioning scientific assumptions: some lessons from rare earth and actinide metals**

*Professor William Evans, University of California, Irvine*

9 April 2018

# References


1 B. Dunn, H. Kamath, J. Tarascon, B. Dunn and H. Kamath, 2011, **334**, 928–935.

2 I. P. on C. Change, in *Climate Change 2013 - The Physical Science Basis*, ed. Intergovernmental Panel on Climate Change, Cambridge University Press, Cambridge, 2014, pp. 1–30.

3 IEA, *Key World Energy Statistics 2016*, 2017.

4 British Petroleum, *Br. Pet.*, 2017, 1–52.

5 J. T. Houghton, G. J. Jenkins and J. J. Ephraums, *Ipcc*, 1990, 1, 414.

6 J.-Y. Hwang, S.-T. Myung and Y.-K. Sun, *Chem. Soc. Rev.*, 2017, **46**, 3529–3614.

7 WebElements, Litihum: the essentials, https://www.webelements.com/lithium/.

8 METALARY, Lithium Price 2019, https://www.metalary.com/lithium-price/, (accessed 3 October 2019).

9 H. Pan, Y.-S. Hu and L. Chen, *Energy Environ. Sci.*, 2013, **6**, 2338.

10 D. Linden and T. B. Reddy, in *Linden's Handbook of Batteries*, 2011, pp. 1.3-1.17.

11 J. R. Owen, *Chem. Soc. Rev.*, 1997, **26**, 259–267.

12 C. Simpson, *Natl. Semicond.*, 2011, 1–12.

13 M. Winter, J. O. Besenhard, M. E. Spahr and P. Novák, *Adv. Mater.*, 1998, **10**, 725–763.

14 D. Aurbach, *Electrochim. Acta*, 2002, **47**, 3561.

15 A. Kraytsberg and Y. Ein-Eli, *J. Solid State Electrochem.*, 2017, **21**, 1907–1923.

16 N. Yamakawa, M. Jiang and C. P. Grey, *Chem. Mater.*, 2009, **21**, 3162–3176.

17 M. R. Palacín, *Chem. Soc. Rev.*, 2009, **38**, 2565.

18 J.-M. Tarascon, P. Poizot, S. Laruelle, S. Grugeon and L. Dupont, *Nature*, 2000, **407**, 496–499.

19 F. Wang, R. Robert, N. A. Chernova, N. Pereira, F. Omenya, F. Badway, X. Hua, M. Ruotolo, R. Zhang, L. Wu, V. Volkov, D. Su, B. Key, M. Stanley Whittingham, C. P. Grey, G. G. Amatucci, Y. Zhu and J. Graetz, *J. Am. Chem. Soc.*, 2011, **133**, 18828–18836.

20 O. Delmer, P. Balaya, L. Kienle and J. Maier, *Adv. Mater.*, 2008, **20**, 501–505.

21 R. R. Heikes and W. D. Johnston, *J. Chem. Phys.*, 1957, **26**, 582–587.

22 M. N. Obrovac and V. L. Chevrier, *Chem. Rev.*, 2014, **114**, 11444–11502.

23 M. T. McDowell, S. W. Lee, W. D. Nix and Y. Cui, *Adv. Mater.*, 2013, **25**, 4966–4985.

24 M. Lao, Y. Zhang, W. Luo, Q. Yan, W. Sun and S. X. Dou, *Adv. Mater.*, 2017, **29**, 1–23.

25 E. Peled, *J. Electrochem. Soc.*, 1979, **126**, 2047.

26 R. D. Rauh, T. F. Reise and S. B. Brummer, *J. Electrochem. Soc.*, 1978, **125**, 186.

27 P. B. Balbuena and Y. Wang, in *Lithium-Ion Batteries*, 2004, vol. 1, pp. 1–3.

28 S. J. An, J. Li, C. Daniel, D. Mohanty, S. Nagpure and D. L. Wood, *Carbon N. Y.*, 2016, **105**, 52–76.

29 Y. W. Perla B. Balbuena, in *Lithium-Ion Batteries*, 2004, pp. 3–7.

30 A. M. Haregewoin, A. S. Wotango and B.-J. Hwang, *Energy Environ. Sci.*, 2016, **9**, 1955–1988.

31 X. H. Liu, L. Zhong, S. Huang, S. X. Mao, T. Zhu and J. Y. Huang, *ACS Nano*, 2012, **6**, 1522–1531.

32 M. Armand, *Solid State Ionics*, 1983, **9**–**10**, 745–754.

33 J. B. Goodenough and Y. Kim, *Chem. Mater.*, 2010, 22, 587–603.

34 R. Marom, S. F. Amalraj, N. Leifer, D. Jacob and D. Aurbach, *J. Mater. Chem.*, 2011, **21**, 9938.

35 G. E. Blomgren, in *Linden's Handbook of Batteries*, 2011, pp. 7.1-7.12.

36 D. Yaakov, Y. Gofer, D. Aurbach and I. C. Halalay, *J. Electrochem. Soc.*, 2010, **157**, A1383.

37 N. Nitta, F. Wu, J. T. Lee and G. Yushin, *Mater. Today*, 2015, **18**, 252–264.

38 N. Yabuuchi, K. Kubota, M. Dahbi and S. Komaba, *Chem. Rev.*, 2014, **114**, 11636–11682.

39 C. Delmas, M. Ménétrier, L. Croguennec, I. Saadoune, A. Rougier, C. Pouillerie, G. Prado, M. Grüne and L. Fournès, *Electrochim. Acta*, 1999, **45**, 243–253.

40 A. Jain, S. P. Ong, G. Hautier, W. Chen, W. D. Richards, S. Dacek, S. Cholia, D. Gunter, D. Skinner, G. Ceder and K. a. Persson, *APL Mater.*, 2013, **1**, 11002.

41 H. Xia, Z. Luo and J. Xie, *Prog. Nat. Sci. Mater. Int.*, 2012, **22**, 572–584.

42 W.-J. Zhang, *J. Power Sources*, 2011, **196**, 2962–2970.

43 M. S. Whittingham, *Chem. Rev.*, 2004, **104**, 4271–4301.

44 J. Qian, W. A. Henderson, W. Xu, P. Bhattacharya, M. Engelhard, O. Borodin and J. G. Zhang, *Nat. Commun.*, 2015, **6**, 6362.

45 P. K. Nayak, L. Yang, W. Brehm and P. Adelhelm, *Angew. Chemie - Int. Ed.*, 2018, **57**, 102–120.

46 S. Chen, Y. Xin, Y. Zhou, Y. Ma, H. Zhou and L. Qi, *Energy Environ. Sci.*, 2014, **7**, 1924.

47 J. Wang, *J. Electrochem. Soc.*, 1986, **133**, 457.

48 U. Kasavajjula, C. Wang and A. J. Appleby, *J. Power Sources*, 2007, **163**, 1003–

1039.

49 M. Mortazavi, Q. Ye, N. Birbilis and N. V. Medhekar, *J. Power Sources*, 2015, **285**, 29–36.

50 M. D. Slater, D. Kim, E. Lee and C. S. Johnson, *Adv. Funct. Mater.*, 2013, **23**, 947–958.

51 T. B. Reddy and D. Linden, *Linden's Handbook of Batteries*, McGraw Hill, Fourth., 2010.

52 1968, US3413150 A.

53 M. Okoshi, Y. Yamada, A. Yamada and H. Nakai, *J. Electrochem. Soc.*, 2013, **160**, A2160–A2165.

54 S. P. Ong, V. L. Chevrier, G. Hautier, A. Jain, C. Moore, S. Kim, X. Ma and G. Ceder, *Energy Environ. Sci.*, 2011, **4**, 3680–3688.

55 C. DELMAS, J. BRACONNIER, C. FOUASSIER and P. HAGENMULLER, *Solid State Ionics*, 1981, **3**–**4**, 165–169.

56 Y. Mo, S. P. Ong and G. Ceder, *Chem. Mater.*, 2014, **26**, 5208–5214.

57 K. Kang and G. Ceder, *Phys. Rev. B*, 2006, **74**, 094105.

58 A. Mendiboure, C. Delmas and P. Hagenmuller, *J. Solid State Chem.*, 1985, **57**, 323–331.

59 J. M. Paulsen and J. R. Dahn, *Solid State Ionics*, 1999, **126**, 3–24.

60 L.-Q. Mu, Y.-S. Hu and L.-Q. Chen, *Chinese Phys. B*, 2015, **24**, 038202.

61 S. Komaba, Y. Matsuura, T. Ishikawa, N. Yabuuchi, W. Murata and S. Kuze, *Electrochem. commun.*, 2012, **21**, 65–68.

62 H. Kim, I. Park, D. H. Seo, S. Lee, S. W. Kim, W. J. Kwon, Y. U. Park, C. S. Kim, S. Jeon and K. Kang, *J. Am. Chem. Soc.*, 2012, **134**, 10369–10372.

63 P. Moreau, D. Guyomard, J. Gaubicher and F. Boucher, *Chem. Mater.*, 2010, **22**, 4126–4128.

64 A. K. Padhi, K. S. Nanjundaswamy and J. B. Goodenough, *J. Electrochem. Soc.*, 1997, **144**, 1188–1194.

65 J. Kim, D. H. Seo, H. Kim, I. Park, J. K. Yoo, S. K. Jung, Y. U. Park, W. A. Goddard and K. Kang, *Energy Environ. Sci.*, 2015, **8**, 540–545.

66 C. Masquelier and L. Croguennec, *Chem. Rev.*, 2013, 113, 6552–6591.

67 N. Recham, J.-N. Chotard, L. Dupont, K. Djellab, M. Armand and J.-M. Tarascon, *J. Electrochem. Soc.*, 2009, **156**, A993.

68 Y. Kawabe, N. Yabuuchi, M. Kajiyama, N. Fukuhara, T. Inamasu, R. Okuyama, I. Nakai and S. Komaba, *Electrochem. commun.*, 2011, **13**, 1225–1228.

69 K. Chihara, N. Chujo, A. Kitajou and S. Okada, *Electrochim. Acta*, 2013, **110**, 240–246.

70 R. Raccichini, A. Varzi, S. Passerini and B. Scrosati, *Nat. Mater.*, 2015, **14**, 271–279.

71 Y. Cao, L. Xiao, M. L. Sushko, W. Wang, B. Schwenzer, J. Xiao, Z. Nie, L. V. Saraf, Z. Yang and J. Liu, *Nano Lett.*, 2012, **12**, 3783–3787.

72 K. Nobuhara, H. Nakayama, M. Nose, S. Nakanishi and H. Iba, *J. Power Sources*, 2013, **243**, 585–587.

73 B. Jache and P. Adelhelm, *Angew. Chemie Int. Ed.*, 2014, **53**, 10169–10173.

74 P. Senguttuvan, G. Rousse, V. Seznec, J.-M. Tarascon and M. R. Palacín, *Chem. Mater.*, 2011, **23**, 4109–4111.

75 H. Kim, H. Kim, Z. Ding, M. H. Lee, K. Lim, G. Yoon and K. Kang, *Adv. Energy Mater.*, 2016, **6**, 1–38.

76 Z. Li, J. Ding and D. Mitlin, *Acc. Chem. Res.*, 2015, **48**, 1657–1665.

77 A. Darwiche, C. Marino, M. T. Sougrati, B. Fraisse, L. Stievano and L. Monconduit, *J. Am. Chem. Soc.*, 2012, **134**, 20805–20811.

78 J. W. Wang, X. H. Liu, S. X. Mao and J. Y. Huang, *Nano Lett.*, 2012, **12**, 5897–

5902.

79 M. Mayo and A. J. Morris, , DOI:10.1021/acs.chemmater.6b04914.

80 P. K. Allan, J. M. Griffin, A. Darwiche, O. J. Borkiewicz, K. M. Wiaderek, K. W. Chapman, A. J. Morris, P. J. Chupas, L. Monconduit and C. P. Grey, *J. Am. Chem. Soc.*, 2016, **138**, 2352–2365.

81 H. Hou, M. Jing, Y. Yang, Y. Zhang, W. Song, X. Yang, J. Chen, Q. Chen and X. Ji, *J. Power Sources*, 2015, **284**, 227–235.

82 Y. Yang, X. Yang, Y. Zhang, H. Hou, M. Jing, Y. Zhu, L. Fang, Q. Chen and X. Ji, *J. Power Sources*, 2015, **282**, 358–367.

83 I. A. Courtney, W. R. McKinnon and J. R. Dahn, *J. Electrochem. Soc.*, 1999, **146**, 59.

84 A. Trifonova, M. Wachtler, M. Winter and J. O. Besenhard, *Ionics (Kiel).*, 2002, **8**, 321–328.

85 L. Xiao, Y. Cao, J. Xiao, W. Wang, L. Kovarik, Z. Nie and J. Liu, *Chem. Commun. Chem. Commun*, 2012, **48**, 3321–3323.

86 C. Marino, M. T. Sougrati, B. Gerke, R. Pöttgen, H. Huo, M. Ménétrier, C. P. Grey and L. Monconduit, *Chem. Mater.*, 2012, **24**, 4735–4743.

87 M. T. Sougrati, J. Fullenwarth, A. Debenedetti, B. Fraisse, J. C. Jumas and L. Monconduit, *J. Mater. Chem.*, 2011, **21**, 10069.

88 B. MALAMAN and J. STEINMETZ, *J. Less-Common Met.*, 1979, **65**, 285–288.

89 E. Dashjav and H. Kleinke, *J. Solid State Chem.*, 2003, **176**, 329–337.

90 K. E. Johnston, M. T. Sougrati, L. Stievano, A. Darwiche, N. Dupré, C. P. Grey and L. Monconduit, *Chem. Mater.*, 2016, **28**, 4032–4041.

91 M. J. Duer, *Introduction to Solid-State NMR Spectroscopy*, 2004.

92 D. C. Apperley, R. K. Harris and P. Hodgkinson, *Solid-State NMR: Basic Principles and Practice*, 2012.

93 K. E. Johnston, M. T. Sougrati, L. Stievano, A. Darwiche, N. Dupre, C. P. Grey and L. Monconduit, *Chem. Mater.*, 2016, **28**, 4032–4041.

94 H. A. Wilhelm, C. Marino, A. Darwiche, L. Monconduit and B. Lestriez, *Electrochem. commun.*, 2012, **24**, 89–92.

95 J. M. Stratford, M. Mayo, P. K. Allan, O. Pecher, O. J. Borkiewicz, K. M. Wiaderek, K. W. Chapman, C. J. Pickard, A. J. Morris and C. P. Grey, *J. Am. Chem. Soc.*, 2017, **139**, 7273–7286.